

RESEARCH

Open Access



# Kidins220-deficient hydrocephalus mice exhibit altered glial phenotypes and AQP4 differential regulation in the retina and optic nerve, with preserved retinal ganglion cell survival

Jose A. Fernández-Albarral<sup>1,2,4†</sup>, Ana Simón-García<sup>5,6†</sup>, Elena Salobrar-García<sup>1,2,4</sup>, Juan J. Salazar<sup>1,2,4</sup>, Celia López-Menéndez<sup>5,6</sup>, Luis S. M. Pajuelo<sup>5,6</sup>, Jose A. Matamoros<sup>1,2,4</sup>, Rosa de Hoz<sup>1,2,4</sup>, Inés López-Cuenca<sup>1,2,4</sup>, Lorena Elvira-Hurtado<sup>1,2</sup>, Lidia Sanchez-Puebla<sup>1,2,3</sup>, Marina P. Sánchez-Carralero<sup>5,6</sup>, Marina Sanz<sup>5,6</sup>, José M. Ramírez<sup>1,2,3</sup>, Teresa Iglesias<sup>5,6\*</sup> and Ana I. Ramírez<sup>1,2,4\*</sup>

## Abstract

Hydrocephalus, characterized by ventriculomegaly due to cerebrospinal fluid accumulation in the cerebral ventricles, is a co-morbidity factor in several neurodevelopmental, psychiatric and neurodegenerative diseases. Aquaporin-4 (AQP4) is crucial for brain water homeostasis, with *Aqp4* knockout mice showing sporadic ventriculomegaly and increased brain water content. Kinase D interacting substrate of 220 kDa (Kidins220), a transmembrane protein involved in neuronal survival, synaptic activity and neurogenesis, controls AQP4 levels in ependymocytes and brain astrocytes. Indeed, Kidins220 deficiency in mice leads to hydrocephalus by downregulating VPS35, a key component of the retromer complex, and targeting AQP4 to lysosomal degradation. Importantly, the ependymal barrier of idiopathic normal pressure hydrocephalus patients shows a similar downregulation of KIDINS220 and AQP4. In addition, pathogenic variants in the *KIDINS220* gene are linked to SINO syndrome, a rare disorder characterized by spastic paraplegia, intellectual disability, nystagmus, and obesity associated with hydrocephalus and ventriculomegaly. Given the retina's structural and functional similarities to the brain, we hypothesized that Kidins220 deficiency would affect retinal water regulation. However, the diminished

†Jose A. Fernández-Albarral and Ana Simón-García contributed equally as first authors.

Teresa Iglesias, Ana Isabel Ramírez contributed equally as senior authors

\*Correspondence:

Teresa Iglesias  
tiglesias@iib.uam.es

Ana I. Ramírez  
airamirez@med.ucm.es

Full list of author information is available at the end of the article



expression of Kidins220 and VPS35 in the retina of Kidins220-deficient hydrocephalus mice, did not cause edema or downregulate AQP4 in Müller cells. Surprisingly, there was an increase in AQP4 levels within this glial cell population. Conversely, AQP4 expression in the optic nerve astrocytes was reduced, as observed in brain astrocytes, suggesting a distinctive adaptive response to hydrocephalus in Müller glia within the Kidins220-deficient retina. Furthermore, we observed phenotypic modifications in retinal glia in Kidins220-deficient hydrocephalus mice. However, we did not find any signs of neuronal damage in the retina. Future studies using OCT and OCTA in SINO syndrome patients with ventriculomegaly will be essential in elucidating the relationship between *KIDINS220* pathogenic variants, retinal alterations, papilledema, and visual function.

**Keywords** Retina, AQP4, Ventriculomegaly, Hydrocephalus, Kidins220, VPS35, SNX27-retromer, Astrocyte hypertrophy, Phagocytic Microglia, Optic nerve, OCT, OCT angiography

## Introduction

Hydrocephalus is a condition characterized by an increase in the volume of the brain ventricles, or ventriculomegaly, caused by the accumulation of cerebrospinal fluid (CSF). Ventriculomegaly is also a co-morbidity factor in several psychiatric and neurodegenerative diseases, including schizophrenia, Parkinson's disease, and Alzheimer's disease [1–3]. Despite this, the pathogenic mechanisms and the molecular and cellular processes related to ventricular enlargement remain largely unknown.

The water channel aquaporin-4 (AQP4) plays a critical role controlling whole-brain water homeostasis. This is evidenced by the presence of sporadic ventriculomegaly, accelerated progression of induced hydrocephalus and increased basal brain water accumulation in AQP4 knockout mice [4–7].

Kinase D interacting substrate of 220 kDa (Kidins220) [8], also known as ankyrin-repeat rich membrane spanning (ARMS) [9], is a transmembrane protein effector of diverse receptors and signaling pathways promoting neuronal survival, differentiation and synaptic activity [10, 11], as well as adult neurogenesis [12]. Alterations in Kidins220 have been found in neurological and neurodegenerative disorders, including cerebral ischemia, Alzheimer's disease, and Huntington's disease [13–18].

Kidins220 has been recently identified as a critical determinant in the control of brain water homeostasis and hydrocephalus development by molecular mechanisms regulating AQP4 turnover [19]. AQP4 is regulated by the sorting nexin 27 (SNX27)-retromer, a complex which facilitates AQP4 endosome-to-plasma membrane recycling and avoids its lysosomal degradation [19]. Kidins220 deficiency downregulates the levels of vacuolar protein sorting 35 (VPS35) and SNX27, key components of the SNX27-retromer complex [20], resulting in the degradation of AQP4 at lysosomes [19]. Consistent with this, Kidins220-deficient mice (*Kidins220<sup>ff</sup>*) exhibit ventriculomegaly and loss of AQP4, SNX27 and VPS35 in the ventricular ependymal layer and brain astrocytes [19]. In addition, the ventricular ependymal lining of idiopathic normal pressure hydrocephalus (iNPH) patients presents

reduced levels of both *KIDINS220* and AQP4 [19]. Further underscoring *KIDINS220* involvement in the pathogenesis of human hydrocephalus, novel variants of the *KIDINS220* gene are linked to schizophrenia [21, 22] and SINO syndrome, a rare disorder characterized by spastic paraplegia, intellectual disability, nystagmus, and obesity [23–25], both diseases associated with ventriculomegaly.

The retina, considered an extension of the brain, could undergo structural and functional changes in cases of Kidins220 deficiency, similar to those observed in the brain. The retina is composed of multiple layers with various cell types, including the retinal pigment epithelium, neuronal elements (photoreceptors, bipolar cells, horizontal cells, amacrine cells, and ganglion cells), and glial cells (Müller glia, astrocytes, and microglia) [26]. Like in the brain, aquaporins (AQPs) play a crucial role in maintaining ionic and osmotic balance in the neurosensory retina. Nine types of AQPs have been identified in human and rodent retinal tissue, with AQP1 and AQP4 being the most abundant [27–29]. AQP4 is expressed in both the retina and the optic nerve (ON), but its presence in the retina is restricted to Müller glia and astrocytes. In the retina, AQP4 is predominantly found in the terminal feet of Müller glia that are in contact with the vitreous or capillary endothelium [27, 30, 31]. This specific expression in Müller glia indicates a crucial role in water management within the retina, directing the osmotic flow of water towards the vitreous and vessels rather than the subretinal space [31, 32]. Notably, large CSF molecules can penetrate the ON but not the retina in mice, indicating the presence of distinct mechanisms governing CSF dynamics in these two tissues [33].

In the retina, upon neuronal activation, potassium ions ( $K^+$ ) are released into the extracellular space. Müller cells capture these ions through their  $K^+$  channels and subsequently release them into the blood through Kir4.1 channels at the perivascular processes of Müller cells. Simultaneously, water, osmotically coupled to the transglial  $K^+$  current, flows from the retinal parenchyma to the blood through surface AQP4 channels of Müller cells. Thus, Müller cells dehydrate the retinal tissue and regulate the water balance in response to neuronal

activity and synaptic transmission [34]. In mice deficient in AQP4, a decrease in the b-wave potential of the electroretinogram is observed, suggesting that impaired excitation or altered function of bipolar cells is due to the inhibition of rapid water transport through Müller cells and consequently, K<sup>+</sup> transport [35].

To date, no previous studies have examined the impact of *Kidins220* deficiency in the retina or in the ON. Given that a decrease in *Kidins220* is associated with lower levels of AQP4 in hypomorphic *Kidins220<sup>ff</sup>* mice, we anticipated the possibility of retinal edema appearance in these animals. This hypothesis was based on the potential decrease in AQP4 expression, considering that water regulation in the retina relies on these water channels in Müller glia. Contrary to expectations, we did not find signs of edema or downregulation of AQP4 in Müller glia. Instead, there was a notable increase in the expression of these channels within Müller cells. This finding suggests that Müller glia possess a specialized adaptive mechanism aimed at eliminating excess retinal water associated with hydrocephalus to protect retinal tissue and function. Conversely, astrocytes expressing AQP4 in the ON mirrored the behavior of *Kidins220*-deficient brain astrocytes, exhibiting the anticipated downregulation of this water channel.

Additionally, we observed phenotypic modifications in glial cells in both the retina and the ON responding to the context of low *Kidins220* expression. However, *Kidins220*-deficient hydrocephalus mice did not show any signs of neuronal damage in the retina, where retinal neuronal survival was preserved.

## Materials and methods

### Experimental animals

*Kidins220<sup>ff</sup>* mice and Wild-Type (WT) mice in C57BL/6J background were generated in G. Schiavo laboratory [36]. Hydrocephalus and *Kidins220* deficiency in *Kidins220<sup>ff</sup>* mice was discovered and characterized by Del Puerto et al. [19]. Briefly, *Kidins220<sup>ff</sup>* adult mice do not show differences in body weight but present an increment in brain weight compared to their littermates, and both male and female mice develop ventriculomegaly to various extents, from mild to severe [19]. The generation of *Kidins220<sup>ff</sup>* mice involved genetic manipulations that caused significant decreases in *Kidins220* expression in different tissues and brain regions, as we have demonstrated. Thus *Kidins220<sup>ff</sup>* animal constitute a hypomorphic mouse model with a general marked deficiency of this protein [19]. Male 3-month-old *Kidins220<sup>ff</sup>* or WT littermates were employed in independent experiments for comparison purposes. Genotyping was performed by PCR using specific pairs of primers. All animals were produced and housed at the animal care facility at Instituto de Investigaciones Biomédicas Sols-Morreale (IIBM, CSIC-UAM,

Madrid, Spain) and maintained under 12/12 h light-dark cycle and with access to food and water ad libitum in a temperature-controlled environment. Overall mouse health was assessed by daily inspection for signs of discomfort, weight loss or changes in behavior, mobility and feeding or drinking habits. Procedures involving animals had been approved by Institutional (IIBM and CSIC) and local Ethical Committees and were conformed to the appropriate national legislations (RD 53/2013) and the guidelines of the European Commission for the accommodation and care of laboratory animals (revised in Appendix A of the Council of Europe Convention ETS123).

### Magnetic resonance imaging

MRI studies were performed in the High Field MRI and Spectroscopy facility (IIBM, CSIC-UAM) using a Bruker Biospect 7.0-T horizontal-bore system (Bruker Medical GmbH, Ettlingen, Germany), equipped with a 1 H selective birdcage resonator of 23 mm and a Bruker gradient insert with 90 mm of diameter (maximum intensity 36 G/cm). All data were acquired using a Hewlett-Packard console running Paravision software (Bruker Medical GmbH) operating on a Linux platform. *Kidins220<sup>ff</sup>* ( $n=9$ ) and WT ( $n=10$ ) animals were anesthetized by inhalation of oxygen (1 L/min) containing 3% isoflurane and maintained during the experiment employing a mask and 2% isoflurane in O<sub>2</sub>. Animal temperature was maintained at approx. 37 °C with a heating blanket. The respiratory rate of the animals was monitored using a Biotrig physiological monitor (SA Instruments, Stony Brook, NY) and the breathing rate was maintained in 60 +/- 40 bpm. T2-weighted (T2-W) spin-echo anatomical images were acquired with a rapid acquisition with relaxation enhancement (RARE) sequence in axial orientations and the following parameters: TR=2500 ms, TE=44 ms, RARE factor=8, Av=6, FOV=2.3 cm, acquisition matrix=256 × 256, slice thickness=1.00 mm without gap and number of slices=14. To calculate the ventricular volume of each ventricle in mm<sup>3</sup>, the ventricular area was measured in all series of images obtained in MRI-T2W for each animal.

### OCT and OCTA analysis

The spectral-domain optical coherence tomography (SD-OCT) examination was performed in *Kidins220<sup>ff</sup>* ( $n=9$ ) and WT ( $n=10$ ) under general anesthesia induced by intraperitoneal injection. Anesthesia was administered as a combination of ketamine (75 mg/kg; Anesketin®, Dechra Veterinary Products SLU, Barcelona, Spain) and medetomidine (0.26 mg/kg; Medetor®, Virbac España S.A., Barcelona, Spain). This anesthesia was reversed by the antagonist atipamezole (Antisedan, 5 mg/mL; Pfizer).

To maintain basal body temperature, mice were housed in cages with a heat source during the recovery period.

In vivo assessment of retinal structures ensued following pupil dilation with tropicamide 10 mg/ml (colircusi tropicamide, Alcon Healthcare, Barcelona, Spain) utilizing the SD-OCT Spectralis equipped with Heidelberg Eye Explorer software for animals v7.0.4 (Heidelberg Engineering, Heidelberg, Germany). During exploration, heating pads were employed to prevent a reduction in body temperature. The cornea was maintained moisturized with topical application of cross-linked sodium hyaluronate (VisuXL<sup>®</sup>, Visufarma SpA, Rome, Italy).

Given the small size of the murine eye in comparison to humans, a +25-diopter optical lens was integrated with the OCT camera (Heidelberg, Germany). Additionally, a polymethyl methacrylate (PMMA) contact lens (3.2 mm diameter, base curve 1.7; VERAPERME VET, Interlenco, Madrid, Spain) was applied to the murine eye to establish a uniform refractive surface.

The measurement beam was meticulously aligned to center the optic nerve head (ONH) within the OCT analysis. Real-time eye tracking was activated to offset minor eye movements, including those arising from respiration or motion artifacts.

An expert investigator manually reviewed and corrected all segmentations. Retinal thickness was stratified into predefined areas in accordance with the Early Treatment Diabetic Retinopathy Study (ETDRS) guidelines, following the methodology described by Salobar-Garcia et al. (2021) [37]. Three concentric rings with a total diameter of 3 mm and centered on the optic nerve were used (Supplementary Fig. 1). The central 1 mm ring (C0), which corresponded to the entrance of the large blood vessels in the mouse retina, was excluded from the analysis, leaving two rings: an inner ring with a 2 mm diameter and an outer ring with a 3 mm diameter. Furthermore, these rings were divided into four quadrants: superior (S), inferior (I), nasal (N) and temporal (T); and these quadrants were divided into inner (S1, I1, N1, T1) and outer (S2, I2, N2, T2) sectors. As for the retinal nerve fiber layer (RNFL) thickness analysis, the results were presented in six sectors: inferior-nasal (IN), nasal (N), superior-nasal (SN), superior-temporal (ST), temporal (T) and inferior-temporal (IT). Only the left eye was analyzed in this study.

The optical coherence tomography angiography (OCTA) images were acquired using the Spectralis II OCT Angiography animal module (Heidelberg Engineering, Heidelberg, Germany). The retinal vasculature was analyzed using an angle of 20° × 20°, a lateral resolution of 4,08 × 3,87 μm/pixel and a total of 512 β-Scans (Supplementary Fig. 1).

All images underwent examination, and those featuring artifacts such as defocus, shadows, or suboptimal

segmentation were eliminated. The images of satisfactory quality were exported in TIFF format for subsequent analysis utilizing the AngioTool software. AngioTool (version 0.6a; National Institutes of Health, National Cancer Institute, Bethesda, MD, USA) was developed as a streamlined tool for angiogenesis analysis. It facilitates the examination of various vascular morphometric parameters, including vessel area, total number of junctions, junction density, average vessel length, total number of ends, and lacunarity. Notably, AngioTool conducts vascular analysis without segmenting the retina and assesses the entirety of the OCTA image. The principle underlying the analysis of OCTA images using AngioTool has been previously described in the works of Zudaire et al. (2011) and López-Cuenca et al. (2022) [38, 39].

### Immunostaining

*Kidins220<sup>ff</sup>* ( $n=6$ ) mice and WT ( $n=6$ ) mice were anesthetized with an i.p injection of medetomidine (Medetor<sup>®</sup>, Virbac España S.A., Barcelona, Spain) and ketamine (Anesketin<sup>®</sup>, Dechra Veterinary Products SLU, Barcelona, Spain) and then transcardially perfused with saline solution followed by 4% paraformaldehyde. Optical cups containing retinas and ON were kept overnight in the same fixative solution after corneas and lens extraction. Next day, optical cups were cryoprotected by immersion in sucrose solutions with increasing concentrations (10%, 20%, and 30%) for 1 h, 2 h, and overnight, respectively, and then embedded in tissue freezing medium (Tissue-Tek<sup>®</sup> O.C.T.<sup>™</sup> Compound, Sakura Finetek Spain, [Barcelona], Spain).

Complete series of 12 μm-thick sagittal sections were obtained by cryostat (Leica Biosystems, [Heidelberg], Germany) from the nasal to temporal retina. Immunostainings were performed in slide-mounted sections incubated in a background solution comprising 2% Triton X-100 and 10% R. T. U Animal-Free Blocker (SP-5035; Vector Laboratories, Inc., [CA], USA) in 0.1 M PBS and then incubated with the appropriate primary antibodies prepared in a solution containing 1% R. T. U Animal-Free Blocker, 2% Triton-X 100, and PBS overnight at 4 °C. In cases where the primary antibody was developed in the same host tissue (mouse), a preliminary step was taken before incubation with the primary antibody to prevent nonspecific reactions, using M.O.M. (Mouse on mouse blocking reagent) from Vector Laboratories, Inc., [CA], USA. Sections were then incubated with secondary antibodies, prepared in PBS 0.1 M, overnight at 4°C. Finally, sections were mounted using Vectashield Vibrance Antifade<sup>®</sup> medium with DAPI (Ref. H-1800; Vector Laboratories, [CA], USA).

Immunostained slides were examined using a Zeiss Axio Imager M.2 fluorescence microscope (Carl Zeiss AG, Oberkochen, Germany) equipped with the

Apotome-2 module (Carl Zeiss AG, Oberkochen, Germany) and a high-resolution Axio Cam 503 Mono camera (Carl Zeiss AG, Oberkochen, Germany). The microscope utilized a Zeiss 10 filter set for Alexa Fluor 488, a Zeiss 64 filter set for Alexa Fluor 594, and a 49-filter set for Alexa Fluor 405. Images were captured and analyzed using ZEN2 software (Carl Zeiss AG, Oberkochen, Germany), maintaining consistent lighting conditions and magnifications throughout the capture process. Some images were captured using a Confocal microscope Zeiss LSM 710 laser-scanning microscope (Zeiss, Germany).

Figures were prepared using Adobe Photoshop CS4 Extended 10.0 (Adobe Systems, [CA], USA).

### Quantitative retinal analysis

For quantitative analysis in retina, six non-consecutive cross-sections, from the nasal to temporal retina, were chosen from *Kidins220<sup>ff</sup>* and WT mice ( $n=6$  per genotype). Within each cross-section, three non-adjacent zones corresponding to the superior, central, and inferior retina were analyzed using a 20x magnification objective, representing a retinal area of  $0.3004 \text{ mm}^2$  (Supplementary Fig. 2). All images were captured under uniform conditions, with consistent values for exposure time and excitation intensity, facilitating qualitative comparisons.

To quantify the area occupied by the following antibodies—GFAP, Iba-1, AQP4, VPS35—in the micrographs obtained from the selected cross-sections, a thresholding tool within the MATLAB environment was employed. The thresholds identify pixels corresponding to objects of interest by analyzing grayscale values, enabling their distinction from other regions within the image based on grayscale values. Subsequently, the quantifications were carried out using an algorithm developed by our research team within the MATLAB environment [40].

To quantify the intensity of vimentin staining, a quantitative analysis of the mean gray fluorescence value was performed using the open-source imaging analysis software ImageJ in micrographs obtained from selected retinal cross-sections. Measurements were performed using a  $100 \times 50$  pixel ROI at the level of the NFL/GCL where the end-feet of Müller cells are located.

Quantification of Iba-1+ cells, Iba-1/CD68+ cells, Brn3a+ cells, and caspase 3+ cells was conducted on each selected cross-section using a double-blind procedure. The manual counting was performed utilizing the “Interactive” counting tool in ZEN2 software (Carl Zeiss AG, Oberkochen, Germany). This software is integrated with the Apotome device and the fluorescence microscope.

For quantitative analysis in ON, six non-consecutive cross-sections were chosen from *Kidins220<sup>ff</sup>* and WT mice ( $n=6$  per genotype). Within each ON cross-section, three zones corresponding to the retina, prelaminar (PL) region, and retrolaminar (RL) region were photographed

using a 20x magnification objective. All images were captured under uniform conditions, with consistent values for exposure time and excitation intensity, facilitating qualitative comparisons. Photomicrographs at 10x magnification were also taken to provide an overview of the main regions of the ON and to facilitate the visualization of the staining with the various antibodies used.

For the quantitative analysis of the expression of the following antibodies —AQP4, GFAP, Kidin220, VPS35—in each of the aforementioned ON regions, a quantitative analysis of the mean gray fluorescence value was performed using the open-source imaging analysis software ImageJ. Measurements were performed using a  $200 \times 200$  pixel ROI in the PL region and in the RL region of the ON, as well as at the level of the NFL/GCL in the retinal region closest to the optic nerve head (only for the AQP4 quantification).

### Preparation of protein extracts and immunoblot analysis

Retinas from *Kidins220<sup>ff</sup>* or WT littermates were dissected, frozen in dry ice and homogenized in RIPA buffer (25 mM Tris-HCl, pH 7.6, 1% Triton X-100, 0.5% sodium deoxycholate, 0.1% SDS, 150 mM NaCl) with protease and phosphatase inhibitors. Lysates were centrifuged for 30 min at 14,000 rpm at 4 °C, and resulting supernatant was considered the total lysate soluble fraction. Prior to SDS-PAGE electrophoresis, equal amounts of lysates with sample buffer were treated at 97 °C, except those samples for AQP4 immunoblot analysis that were treated at 37 °C. This temperature shift is crucial since boiling protein samples typically abolishes the ability of AQP4 antibodies to distinguish the different isoforms (M23, M1 and M23-ex) [41]. For immunoblot analysis membranes were incubated with different primary and secondary antibodies (see detailed information in Supplementary Table 1) and immunoreactive bands were detected by ECL (PerkinElmer, Waltham, MA USA). Immunoblot signals were quantified by densitometric analysis with ImageJ 1.47d software (NIH) and normalized using  $\beta$ -actin band signal intensities. Data were expressed relative to values obtained in their respective WT mice.

### Antibodies

AQP4 rabbit polyclonal antibody, and Brn3a, Vimentin and Dystrophin mouse monoclonal antibodies were from Sigma-Aldrich (St Louis, MO, USA). SNTB2 mouse monoclonal antibody, recognizing  $\alpha$ -,  $\beta$ 1-, and  $\beta$ 2-Syntrophin, was from Thermo Fisher Scientific (Massachusetts, USA). GFAP mouse monoclonal antibody was from Millipore (Massachusetts, MA, USA). Kidins220 rabbit polyclonal antibodies were generated in T. Iglesias laboratory as described [8, 42]. VPS35 goat polyclonal antibody was from Abcam (Cambridge, UK). CD68 monoclonal antibody was from BioRad (California,

USA). Caspase-3 rabbit polyclonal antibody was from Cell signaling (Massachusetts, USA). Iba-1 and C3d complement rabbit polyclonal antibodies were from Wako Chemicals (Richmond, USA) and DAKO (Glostrup, Denmark), respectively. Donkey anti-rat Alexa Fluor 488, goat anti-mouse Alexa Fluor 488, goat anti-mouse Alexa Fluor 594, donkey anti-goat Alexa Fluor 488, donkey anti-goat Alexa Fluor 647, donkey anti-rabbit Alexa Fluor 594 and donkey anti-rabbit Alexa Fluor 555 secondary antibodies were from Invitrogen (Thermo Fisher Scientific). Horseradish peroxidase conjugated anti-rabbit secondary antibody was from Invitrogen (Thermo Fisher Scientific) and horseradish peroxidase conjugated anti-mouse secondary antibody was from Rockland (Pottstown, PA, USA). Detailed information about all the above-mentioned antibodies and dilutions used for the different applications is given in Supplementary Table 1.

### Statistical analysis

Statistical analysis was performed using GraphPad Prism v.9 (GraphPad Software, La Jolla, CA, USA), and the same software was utilized for graph design. When the data deviated from a normal distribution, nonparametric tests were employed for analysis. Conversely, when the data conformed to a normal distribution, parametric tests were utilized.

For immunostaining data analysis, the Mann–Whitney U test (for unpaired data) or Wilcoxon W test (for paired data) was employed. Statistical analysis of the volume ( $\text{mm}^3$ ) of the lateral and third ventricles (LV + TV), Sylvius aqueduct (SA) and fourth ventricle (FV) were carried out using unpaired Student's *t*-test. Immunoblot analyses of significant differences between means were carried out using unpaired Student's *t*-test. Results are shown as mean  $\pm$  s.e.m. and differences were considered statistically significant when  $p < 0.05$ . The notations denoting different levels of significance were \*  $p < 0.05$ , \*\*  $p < 0.01$ , \*\*\*  $p < 0.001$ , \*\*\*\*  $p < 0.0001$ .

## Results

### Deficiencies in Kidins220 protein in the retina of Kidins220<sup>ff</sup> hypomorphic mice

In this study we have examined the levels of Kidins220 in the retina, both in wild-type (WT) and Kidins220-deficient hydrocephalus mice (Kidins220<sup>ff</sup>) [19]. First, we corroborated the hydrocephalus phenotype of all Kidins220-deficient animals used for these studies before the obtention of their retinas by magnetic resonance imaging (MRI; Fig. 1).

Immunofluorescence analysis of Kidins220 in the retina revealed a general labelling across the different layers in WT animals, with Kidins220 signal being more intense in the retinal ganglion cell layer (GCL) (Fig. 2A). In contrast, the overall staining of this protein was decreased in

Kidins220<sup>ff</sup> mice (Fig. 2A). Consistent with this observation, immunoblot analysis of protein lysates obtained from retinal tissue showed a significant reduction in Kidins220 levels, (37% decrease) ( $p < 0.01$ ), in samples from Kidins220-deficient mice compared to WT controls (Fig. 2B).

### Kidins220 deficiency does not lead to alterations in retinal thickness or vascular pattern

To examine the effect of Kidins220 deficiency on retinal morphology and microvascular structure, we conducted OCT analysis. The results showed no statistically significant differences in either total retinal thickness (Fig. 3A) or RNFL thickness (Fig. 3B) in any of the sectors analyzed in Kidins220<sup>ff</sup> compared to WT mice (Table 1). Additionally, papilledema was not observed during fundus examination or OCT studies.

We then compared vascular parameters obtained from OCTA between the two study groups (Kidins220<sup>ff</sup> vs. WT) using the AngioTool software. We found no significant changes (Fig. 3C; Table 2), indicating that the reduction in Kidins220 levels does not result in major alterations in the retinal vessels.

### The number of retinal ganglion cells and the incidence of retinal apoptosis do not vary in Kidins220-deficient mice

Kidins220 is known to be a key for neuronal survival pathways [17]. Therefore, we analyzed the number of Brn3a+ retinal ganglion cells (RGC), anticipating a decrease in their number in Kidins220-deficient mice. However, our analysis revealed no significant changes in RGC numbers Kidins220-deficient retinas compared to those of WT mice, whether analyzing the total retina or examining different retinal sectors (peripapillary, intermediate, and peripheral) (Fig. 4). Consistent with this result, we did not detect differences in cell death between the two groups of mice after labelling the retinas with the apoptotic marker for cleaved caspase-3, either in the total retina or in retinal sectors (peripapillary, intermediate, periphery) (Fig. 4).

### Kidins220 deficiency in the retina is associated with changes in retinal astrocytes, Müller glia and microglia

We then examined microglia, astrocytes and Müller glia in the retina using markers for these glial cells to determine possible changes due to Kidins220 deficiency. The retinal area occupied by Iba-1+microglial cells (Iba-1+RA) was significantly increased in Kidins220<sup>ff</sup> animals compared to WT (103% increase) ( $p < 0.0001$ ) (Fig. 5A, B). Similar findings were observed when quantifying the number of Iba-1+ cells in different retinal layers, revealing an increase in the number of Iba-1+ cells in Kidins220<sup>ff</sup> mice retina (Fig. 5A, C). This increase was statistically significant both in the outer plexiform layer

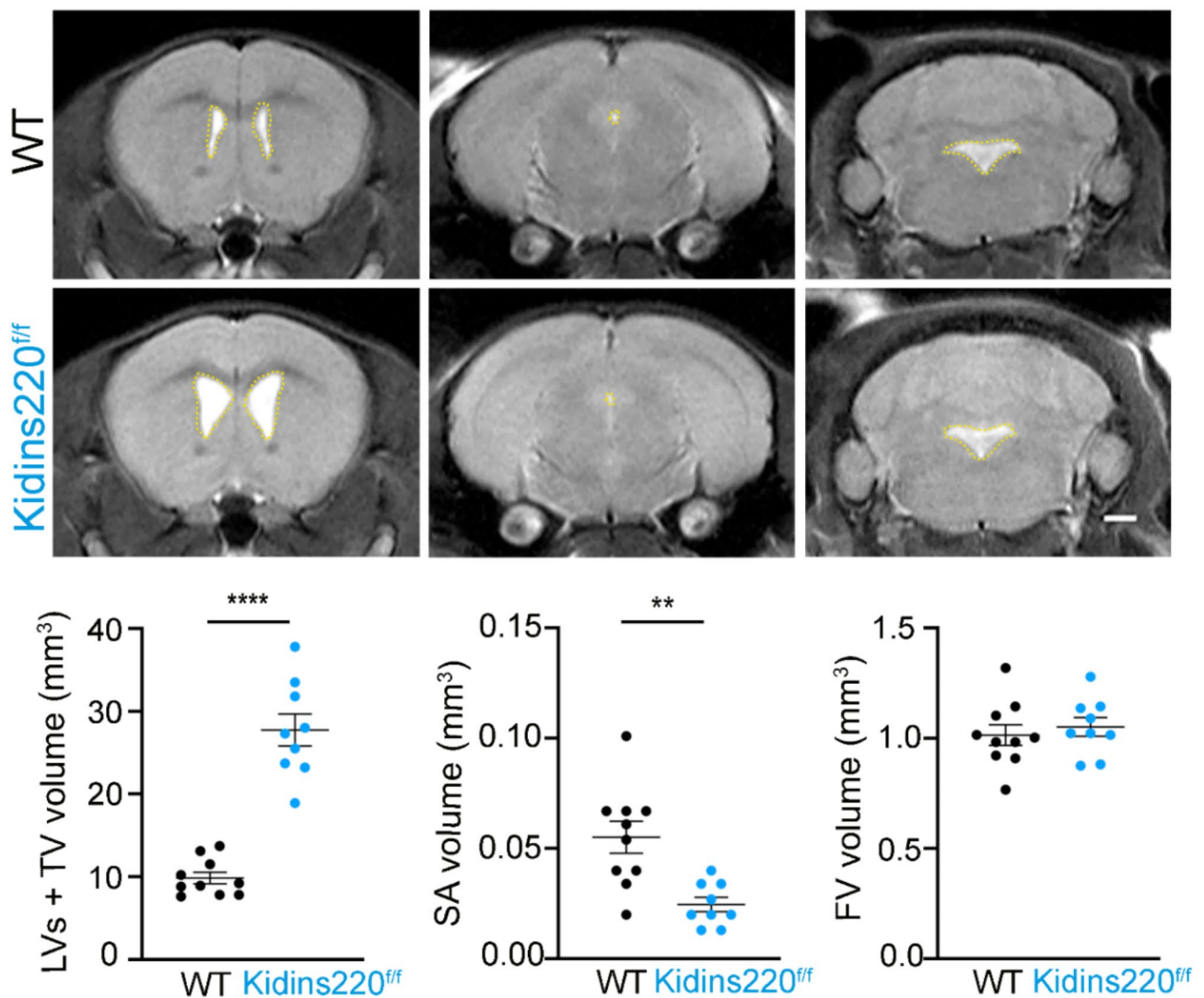


**Fig. 1** Obstructive hydrocephalus in *Kidins220<sup>ff</sup>* deficient mice where retinas have been analyzed. Representative in vivo brain coronal view of T2-weighted (T2-W) magnetic resonance images (MRI) showing lateral and third ventricles (LVs+TV; left panels), aqueduct of Sylvius (SA; central panels) and fourth ventricle (FV; right panels) of 2-month-old WT and *Kidins220<sup>ff</sup>* male mice. Graphs represent the quantification of the volume (mm<sup>3</sup>) of the lateral and third ventricles (LV+TV), Sylvius aqueduct (SA) and fourth ventricle (FV) in WT and *Kidins220<sup>ff</sup>* mice. Each data point denotes one individual. Data are mean  $\pm$  s.e.m. and were analyzed by two-tailed unpaired Student t-test. \*\* $p < 0.01$ , \*\*\*\* $p < 0.0001$ . Scale bar 1 mm

(OPL) (78% increase) ( $p < 0.0001$ ) and in the inner complex layer (ICL) (69.45% increase) ( $p < 0.001$ ), which comprises the inner plexiform layer (IPL), GCL, and nerve fiber layer (NFL). Additionally, Iba-1+/CD68+ phagocytic cells were also more numerous in *Kidins220<sup>ff</sup>* animals compared to WT in the OPL (224.96% increase) and ICL (168.79% increase) ( $p < 0.0001$  for both) (Fig. 5A, D).

*Kidins220<sup>ff</sup>* animals exhibited alterations in retinal astrocytes in response to a context of *Kidins220* deficits, with a statistically significant increase in the retinal area occupied by glial fibrillary acidic protein - GFAP - (GFAP-RA) immunostaining (40.39% increase) ( $p < 0.0001$ ) (Fig. 6A, B). Higher magnification images

might suggest a possible hypertrophic phenotype of *Kidins220*-deficient astrocytes (Fig. 6A, lower panels).

GFAP co-immunostaining with the complement factor C3 further suggested a phenotypic change in astrocytes of the GCL in *Kidins220<sup>ff</sup>* retinas (Supplementary Fig. 3). Additionally, vimentin expressed in astrocytes and Müller glia also augmented in the retina of *Kidins220<sup>ff</sup>* compared to WT mice (23.68% increase) ( $p < 0.0001$ ) (Fig. 7A, B).

#### ***Kidins220*-deficient retina shows an increase in glial AQP4 while exhibiting lower expression of VPS35**

We have previously reported that *Kidins220* deficiency diminishes the levels of the water channel AQP4 and the

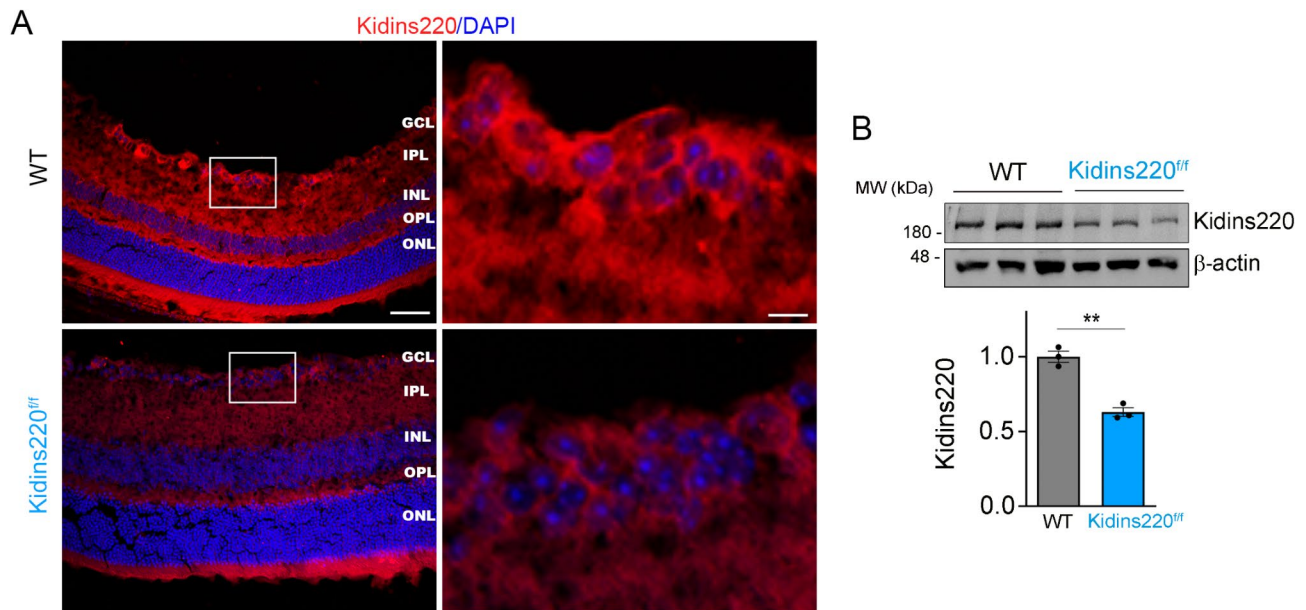


**Fig. 2** Kidins220 levels are decreased in the retina of *Kidins220<sup>ff</sup>* deficient mice. **(A)** Representative fluorescence microscopy images of Kidins220 immunostaining (red) in WT and in *Kidins220<sup>ff</sup>* deficient animals. The different retina layers are indicated. Nuclei are labelled with DAPI (blue). Magnified images (Zoom) are shown in the right panels. **(B)** Representative Kidins220 and b-actin (loading control) immunoblots of retina lysates from WT and *Kidins220<sup>ff</sup>* mice and the corresponding Kidins220 levels quantification graph. Data are mean  $\pm$  s.e.m.; each data point denotes one individual mouse; \*\* $p < 0.01$ , by two-tailed unpaired Student's *t*-test. Abbreviations: ONL (Outer nuclear layer), OPL (Outer plexiform layer), INL (Inner nuclear layer), IPL (Inner plexiform layer), GCL (Ganglion cell layer). Scale bar 50  $\mu$ m, zoom 10  $\mu$ m

key retromer complex component, VPS35, in the ependymal cells lining the brain ventricular walls and astrocytes [19]. We therefore examined whether similar changes were occurring in the retina, as astrocytes and Müller cells also express AQP4. Opposite to what was observed in the brain, immunostaining of AQP4 was increased in Kidins220-deficient retina compared to controls, especially in the layers underneath the GCL (27.26% increase) ( $p < 0.0001$ ) (Fig. 8A, B).

Regarding VPS35, its signal was diffusely expressed in the photoreceptor outer segment layers (OS), OPL, IPL and GCL, with more intensity in the GCL-NFL (Fig. 8A). Consistent with data obtained in the brain, the retinal area occupied by VPS35 immunostaining (VPS35-RA), was significantly lower in the *Kidins220<sup>ff</sup>* group compared to WT, with a more pronounced decrease in the signal observed in the GCL and other retinal layers than in the IPL (61.41% decrease) ( $p < 0.0001$ ) (Fig. 8A, C). Overall, these results suggest that AQP4 retinal upregulation may occur mainly in Müller glia, where VPS35 downregulation is less evident.

We also assessed the expression levels of dystrophin, a molecule that, together with syntrophins, can participate in AQP4 anchoring and is part of the dystrophin-associated complex [43], not finding increases between WT and *Kidins220<sup>ff</sup>* retinas by immunofluorescence analysis (Supplementary Fig. 4). In addition, immunoblot analysis

showed no variations in dystrophin or syntrophin levels (Supplementary Fig. 5).

This result could indicate that Kidins220 deficiency may enhance the upregulation of a pool of retinal AQP4 that is independent of the canonical dystrophin membrane-anchoring complex.

To further support this notion, we next checked for possible variations in AQP4-M23-ex by immunoblot. This AQP4 isoform bears a C-terminal extension and displays a perivascular polarization and expression in dystrophin-dependent pools [41]. According to these authors, that identified M23-ex, immunoblot analysis of unboiled protein extracts can identify three bands corresponding to AQP4 M23 (23 kDa), M1 (32 kDa) and M23-ex (35 kDa). Our analysis of retinal non-boiled lysates from WT and *Kidins220<sup>ff</sup>* mice detected M23, M1 and M23-ex isoforms (Supplementary Fig. 6). However, quantification of the different immunoblot bands did not render significant differences between control and Kidins220-deficient lysates (Supplementary Fig. 6). Together, data could indicate that expression of AQP4 M23-ex is not altered, suggesting that this dystrophin-dependent pool of AQP4 remains preserved in conditions of Kidins220 deficits.

However, AQP4 immunoblot data are in striking contrast to those obtained by immunofluorescence analysis (Fig. 8), suggesting that destruction of tissue compartmentalization by homogenization and lysis for the

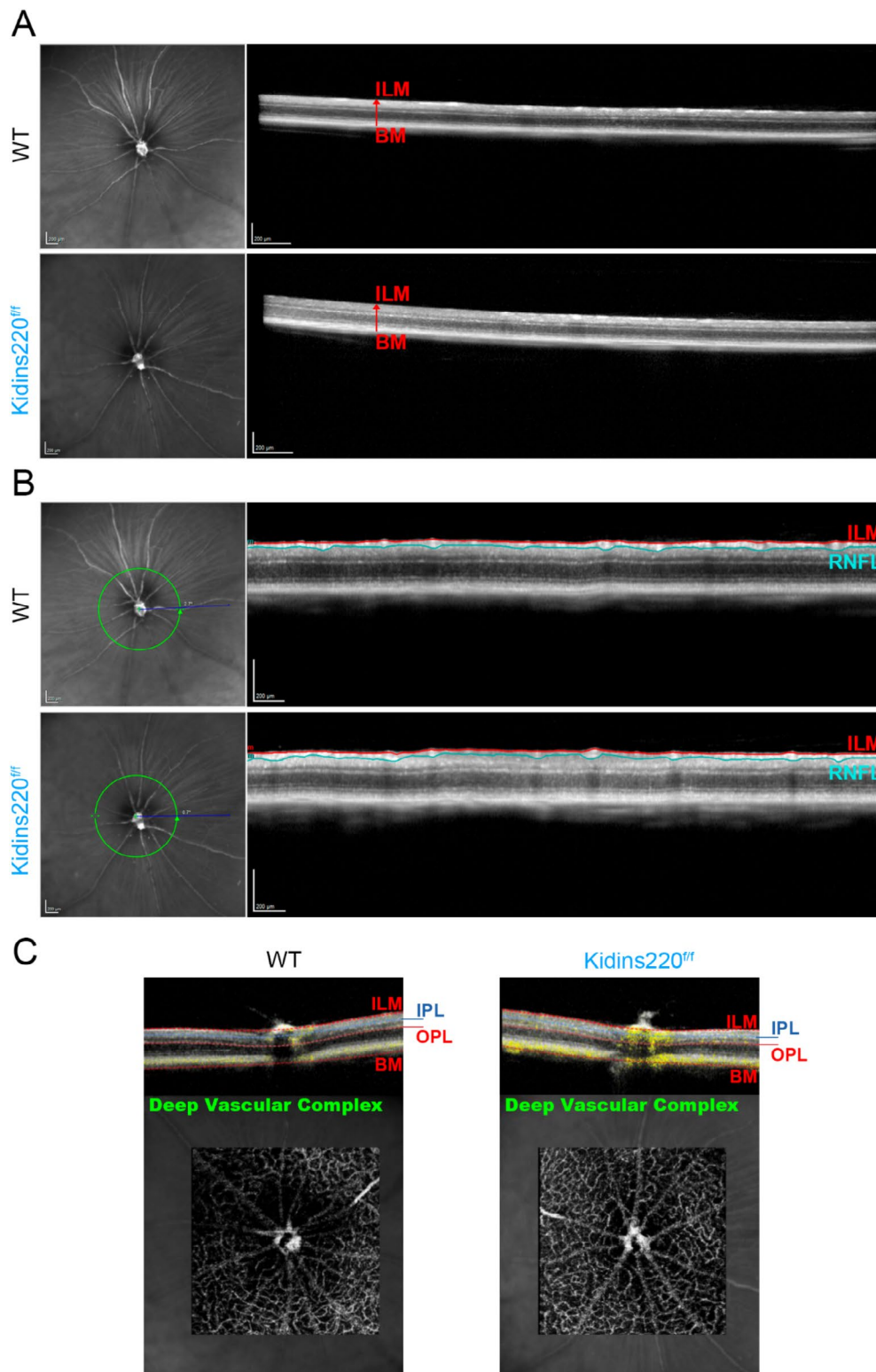


**Fig. 3** *Kidins220<sup>fl/fl</sup>* deficient animals show no major changes in the retina structure and vasculature. **(A)** Representative eye fundus (Left panels) and total retinal thickness measure by OCT (Right panels) of WT and *Kidins220<sup>fl/fl</sup>* mice, with no papilledema observed in *Kidins220*-deficient animals. **(B)** Representative images of the retinal area analyzed for the measurement of the RNFL total thickness (Left panels), and the RNFL total thickness by OCT (Right panels) of WT and *Kidins220<sup>fl/fl</sup>* mice. **(C)** Representative images of deep vascular complex of WT and *Kidins220<sup>fl/fl</sup>* mice by OCTA. Abbreviations: ILM (Inner limiting membrane), BM (Bruch membrane), RNFL (Retinal nerve fiber layer), OCT (Optical Coherence Tomography), OCTA (Optical Coherence Tomography Angiography)

**Table 1** Values of RNFL thickness and total retina thickness measured with OCT

		WT		Kidins220 <sup>ff</sup>		p-value
		n= 10		n= 9		
		Mean	SD	Mean	SD	
RNFL (μm)	S	22.60	4.81	22.67	2.78	0.7619
	I	25.60	1.07	26.67	2.69	0.2803
	N	22.80	3.33	22.89	1.54	0.6295
	T	24.40	2.76	23.89	1.62	0.8649
	SN	22.60	6.02	23.00	2.92	0.5594
	ST	22.40	4.01	22.11	4.37	0.8884
	IN	24.90	2.38	25.67	2.55	0.4785
	IT	26.60	3.17	28.56	3.00	0.2474
	Global	23.90	2.28	24.00	0.87	0.8895
Total Retina (μm)	VOLUME (mm <sup>3</sup> )	1.723	0.02	1.707	0.02	0.1219
	S1	246.00	6.04	242.89	4.91	0.2845
	I1	240.90	4.23	237.67	5.32	0.2851
	N1	240.90	4.12	240.22	2.95	0.7636
	T1	240.30	4.30	239.11	3.66	0.4817
	S2	254.90	4.07	252.22	3.42	0.1866
	I2	244.80	3.26	244.44	2.60	0.7348
	N2	245.40	4.67	245.56	1.74	0.9486
	T2	245.70	3.59	243.67	3.35	0.2482

Mean values ± standard deviation (SD) of RNFL thickness and total retina thickness of different sectors analyzed. Data analyzed via Mann-Whitney U-test. Abbreviations: RNFL (Retinal nerve fiber layer), S (Superior), I (Inferior), N (Nasal), T (Temporal), SN (supero-nasal), ST (supero-temporal), IN (infero-nasal), IT (infero-temporal)

**Table 2** Values of retinal vessels analysis with OCTA

	WT		Kidins220 <sup>ff</sup>		p-value
	n= 10		n= 9		
	Mean	SD	Mean	SD	
Vessel's area	218394.5	6471.1	217954.7	7265.8	0.624
% of vessel area	44.03	1.29	43.95	1.37	0.806
Junctions total number	554.7	66.7	582.6	49.0	0.288
Junctions density	0.00112	0.00014	0.00117	0.00010	0.327
Total vessel length	24618.45	1298.12	25037.84	1061.64	0.327
Mean vessel length	355.9	123.8	402.9	107.1	0.191
Endpoints total number	438.3	57.9	424.8	27.5	0.683
Average lacunarity	0.0579	0.0043	0.0585	0.0053	0.935

Mean values ± standard deviation (SD) of different vascular parameters analyzed in the deep vascular complex. Data analyzed via Mann-Whitney U-test

obtention of soluble protein extracts can give rise to misleading results. This would be the case for the retina and the optic nerve, complex tissues divided in multiple regions and constituted by multiple different cell types. On the contrary, immunofluorescence microscopy allows to perform qualitative and quantitative analysis of these tissues preserving their architecture and regional and cellular identity.

#### The optic nerve of Kidins220-deficient mice presents an increase in GFAP expression accompanied by decreases in AQP4 and VPS35

Compared to the retina, the ON can be more directly influenced by the CSE, and sense changes in CSF pressure in hydrocephalus conditions. The increase in intracranial

pressure caused by CSF excess can lead to elevated pressure in the arachnoid space surrounding the ON [44]. Thus, we hypothesized that the effects of Kidins220 deficiency in the ON could be more similar to those occurring at the ependymal barrier of the brain ventricles.

First we examined Kidins220 and VPS35 labelling in the ON, finding a significant decrease in the expression of both molecules (Fig. 9A-C) in Kidins220<sup>ff</sup> mice compared to WT mice, both in the prelaminar (PL) region (28.39% decrease for Kidins220, 22.80% decrease for VPS35) ( $p < 0.05$  for both) and in the retrolaminar (RL) region (37.84% decrease for Kidins220, 40.60% decrease for VPS35) ( $p < 0.001$  for both).

Next, we analyzed AQP4 in the ON, that showed a heterogeneous immunolabelling in WT mice, with low

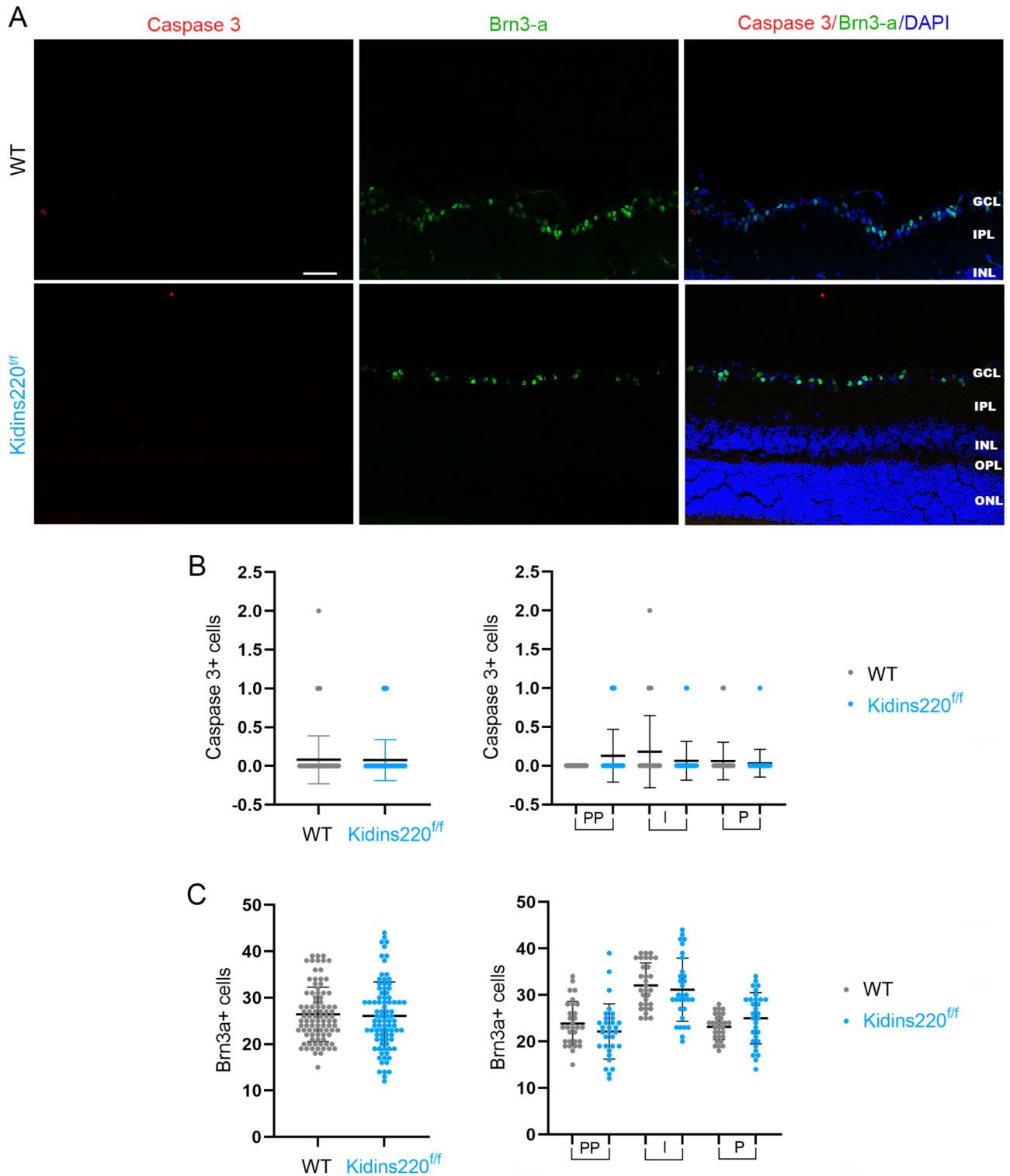


**Fig. 4** Kidins220 deficiency in the retina is not associated with loss of retinal ganglion cells (RGC) or decreases in their survival. **(A)** Representative fluorescence microscopy images of retinas labeled for apoptotic cleaved caspase 3 + cells (red) and cells stained with the RGC specific marker Brn3a (green) in WT and in *Kidins220<sup>ff</sup>* deficient animals. Nuclei are labelled with DAPI (blue). **(B, C)** Quantitative analysis of total number of cleaved caspase 3 + cells and Brn3a + cells, respectively, in the total retina or in different sectors - PP (peripapillary), I (intermediate), and P (peripheral) - in WT and *Kidins220<sup>ff</sup>* animals. Data are mean  $\pm$  s.e.m.; each data point denotes an individual measure of the number of Brn3a + cells in retinal sections of WT and *Kidins220<sup>ff</sup>* animals and were analyzed via Mann-Whitney U-test. Abbreviations: ONL (Outer nuclear layer), OPL (Outer plexiform layer), INL (Inner nuclear layer), IPL (Inner plexiform layer), GCL (Ganglion cell layer). Scale bar 50  $\mu$ m

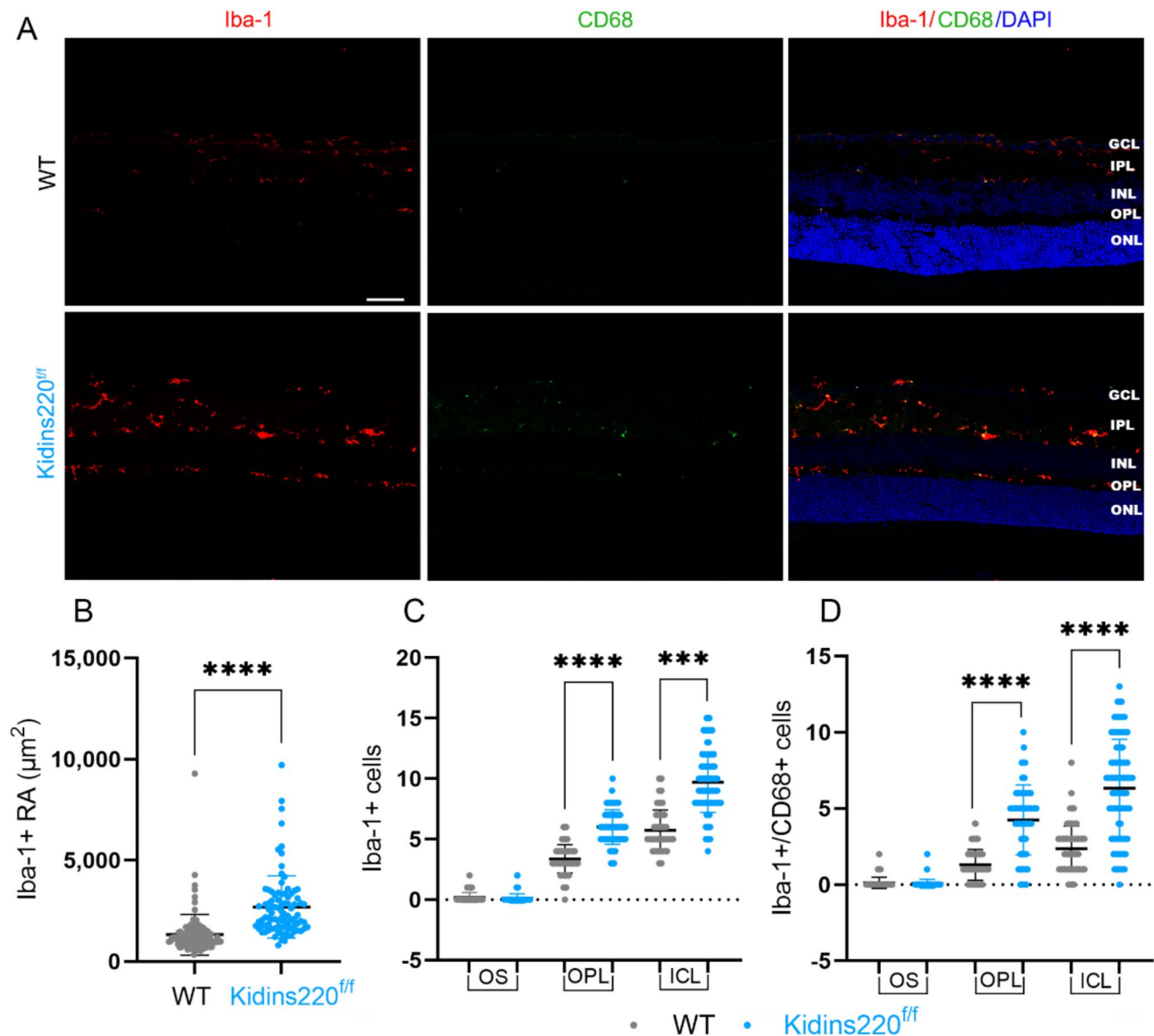


**Fig. 5** Increased phagocytic microglia in the mouse retina with deficits in *Kidins220*. **(A)** Representative fluorescence microscopy images of Iba-1 (red) and CD68 (green) staining to label phagocytic microglia cells in WT and in *Kidins220*<sup>ff</sup> mice. Nuclei are labelled with DAPI (blue). **(B, C, D)** Quantitative analysis of total retinal area (RA) occupied by Iba-1+ immunostaining. **(B)** the number of Iba-1+ cells **(C)** and Iba-1+/CD68+ cells **(D)** in different retina layers - OS (outer segment layer), OPL (outer plexiform layer) and ICL (inner complex layer) in WT and *Kidins220*<sup>ff</sup> animals. Data are mean  $\pm$  s.e.m.; each data point denotes an individual measure of the Iba1 + RA, the number of Iba-1+ cells and the number of Iba-1+/CD68+ cells in retinal sections of WT and *Kidins220*<sup>ff</sup> animals and were analyzed via Mann-Whitney U-test. \*\*\* $p < 0.001$ , \*\*\*\* $p < 0.0001$ . Abbreviations: ONL (Outer nuclear layer), OPL (Outer plexiform layer), INL (Inner nuclear layer), IPL (Inner plexiform layer), GCL (Ganglion cell layer). Scale bar 50  $\mu$ m

expression in the PL and glial lamina cribrosa (GLC) regions, and higher expression in the RL region (Fig. 10A, B). Notably, the expression of AQP4 was significantly decreased in the PL region (11.74% decrease) ( $p < 0.05$ ), being this reduction more pronounced in the RL region (42.23% decrease) ( $p < 0.0001$ ) of the ON in *Kidins220*<sup>ff</sup> mice (Fig. 10A, B). However, when analyzing the retina (R), specifically the NFL/GCL layer closest to the ON head, AQP4 expression was significantly increased (35.97% increase) ( $p < 0.0001$ ) in *Kidins220*<sup>ff</sup> mice.

Furthermore, comparison of AQP4 immunostaining in the retina and the RL region of the ON of *Kidins220*-deficient mice, rendered significant differences (95% increase) ( $p < 0.0001$ ) (Fig. 10A, B).

Regarding GFAP expression, it was significantly augmented in the ON in *Kidins220*-deficient animals in PL (31.06% increase) ( $p < 0.01$ ) and in RL (52.08% increase) ( $p < 0.001$ ), indicative of astrocytic changes associated with *Kidins220* deficiency (Fig. 10A, C).

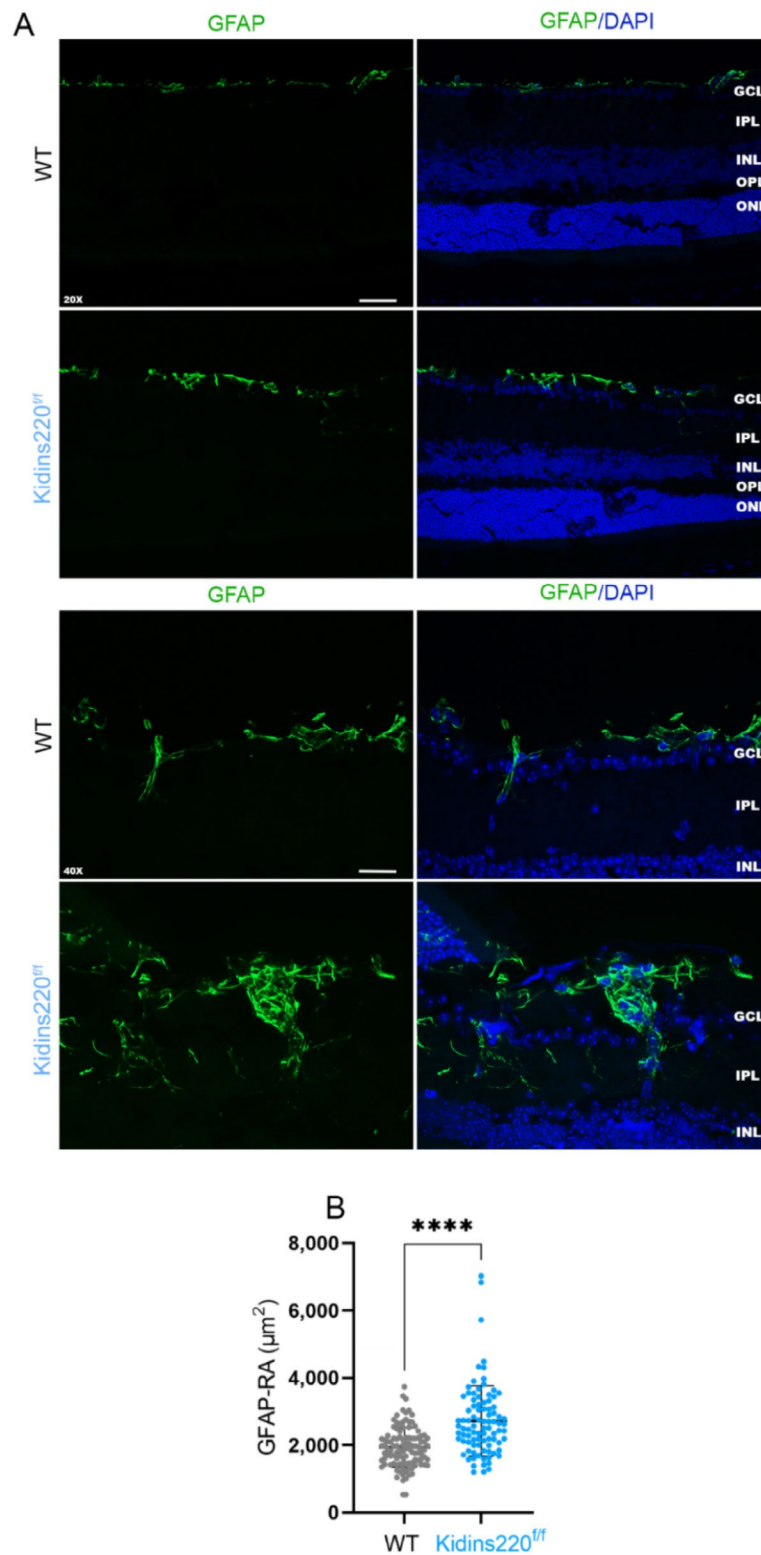


**Fig. 6** Increased GFAP expression in astrocytes of *Kidins220*-deficient retina. **(A)**. Representative fluorescence microscopy images of GFAP + immunolabelling (green) in WT and *Kidins220<sup>fl</sup>* retinas. Nuclei are labelled with DAPI (blue). **(B)**. Quantitative analysis of total retinal area occupied by GFAP + immunostaining (GFAP-RA). Data are mean  $\pm$  s.e.m.; each data point denotes an individual measure of the GFAP-RA in retinal sections of WT and *Kidins220<sup>fl</sup>* animals and were analyzed via Mann-Whitney U-test. \*\*\*\* $p < 0.0001$ . Abbreviations: GFAP (Glial fibrillary acidic protein), ONL (Outer nuclear layer), OPL (Outer plexiform layer), INL (Inner nuclear layer), IPL (Inner plexiform layer), GCL (Ganglion cell layer). Upper panels: Scale bar 50  $\mu\text{m}$  (20X); Lower panels with magnified images: Scale bar 25  $\mu\text{m}$  (40X)

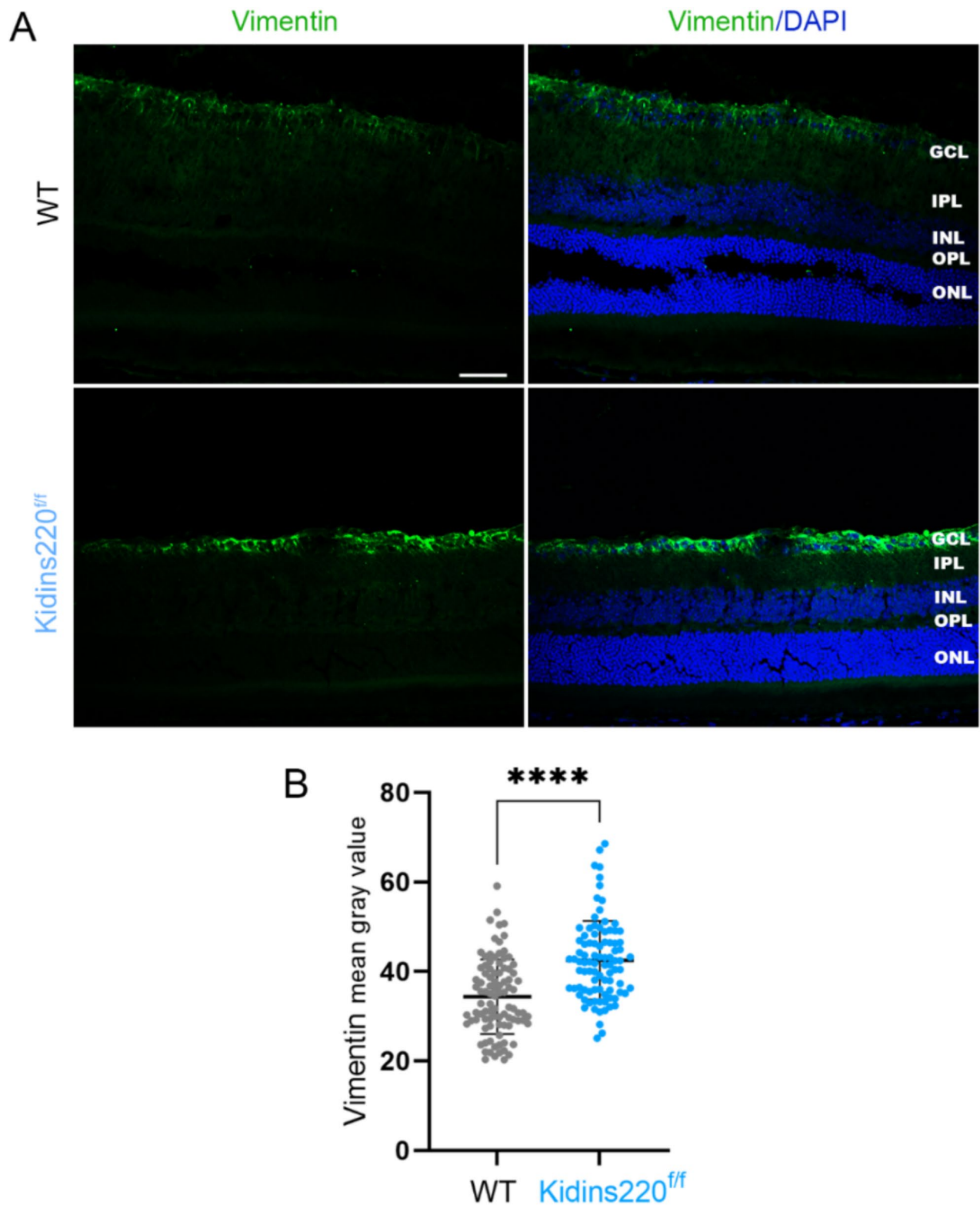


**Fig. 7** Increased expression of vimentin in astrocytes and Müller glia in Kidins220-deficient retina. **(A)**. Representative fluorescence microscopy images of Vimentin + immunolabelling (green) in WT and *Kidins220<sup>ff</sup>* retinas. Nuclei are labelled with DAPI (blue). **(B)**. Quantitative analysis of the mean gray fluorescence value of Vimentin + immunostaining. Data are mean  $\pm$  s.e.m.; each data point denotes an individual measure of the mean gray value in retinal sections of WT and *Kidins220<sup>ff</sup>* animals and were analyzed via Mann-Whitney U-test. \*\*\*\* $p < 0.0001$ . Abbreviations: ONL (Outer nuclear layer), OPL (Outer plexiform layer), INL (Inner nuclear layer), IPL (Inner plexiform layer), GCL (Ganglion cell layer). Scale bar 50  $\mu$ m

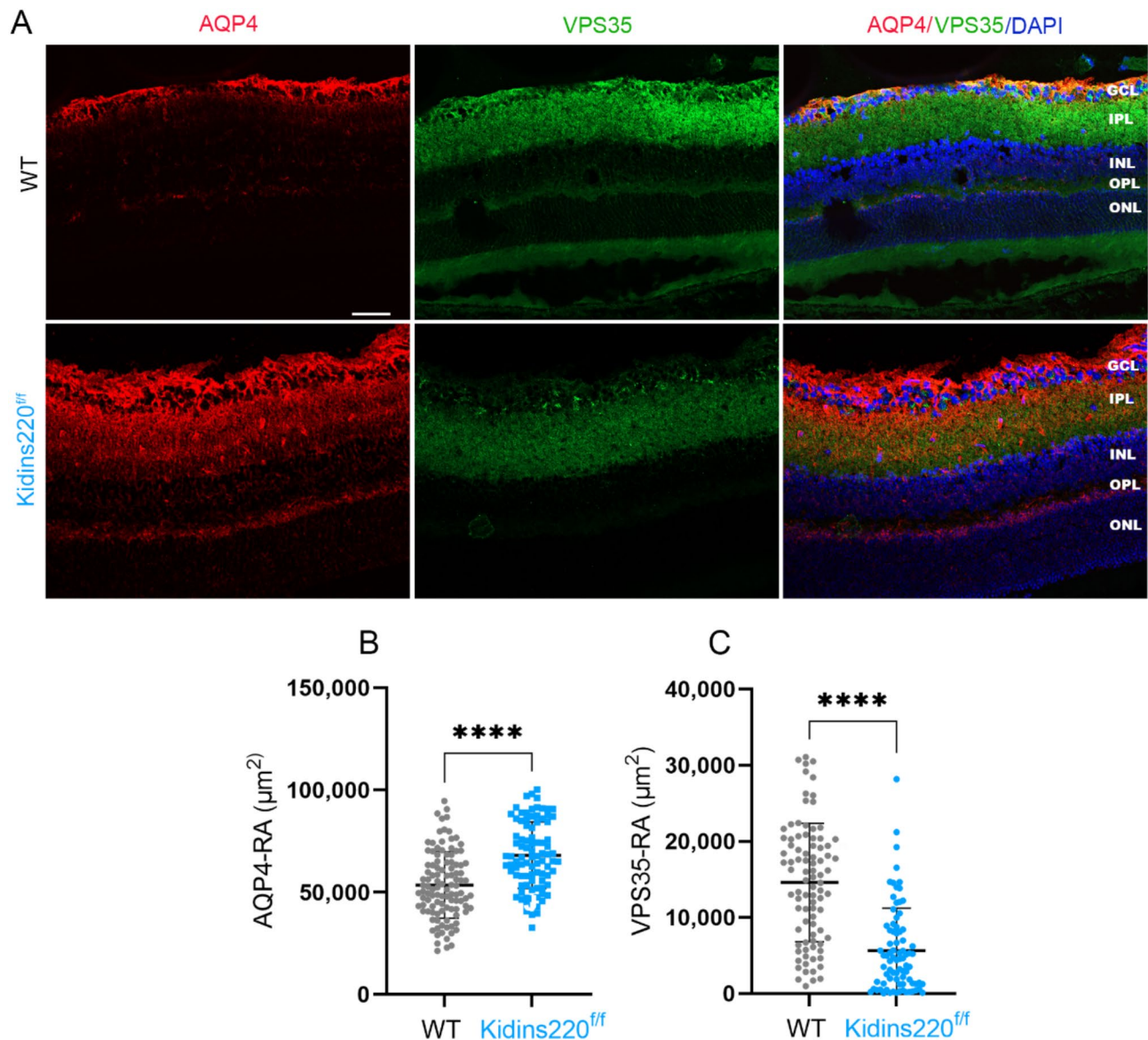


**Fig. 8** Kidins220-deficient retina presents an unexpected increase of AQP4 and low levels of VPS35. **(A)**. Representative fluorescence microscopy images of AQP4 (red) and VPS35 (green) expression in WT and in *Kidins220*<sup>ff</sup> animals. Nuclei are labelled with DAPI (blue). **(B, C)**. Quantitative analysis of total retinal area occupied by AQP4+ (AQP4-RA) **(B)** and VPS35+ (VPS35-RA) **(C)** immunostaining in WT and *Kidins220*<sup>ff</sup> mice. Data are mean ± s.e.m.; each data point denotes an individual measure of the AQP4-RA and the VPS35-RA in retinal sections of WT and *Kidins220*<sup>ff</sup> animals and were analyzed via Mann-Whitney U-test. \*\*\*\**p* < 0.0001. Abbreviations: ONL (Outer nuclear layer), OPL (Outer plexiform layer), INL (Inner nuclear layer), IPL (Inner plexiform layer), GCL (Ganglion cell layer). Scale bar 50 μm

## Discussion

This study is the first to analyze the retinal and ON behavior in a hydrocephalus model caused by *Kidins220* deficiency, using adult *Kidins220*<sup>ff</sup> hypomorphic mice [19]. Consistent with previous findings in various brain structures and other tissues from *Kidins220*<sup>ff</sup> hypomorphic animals [19] we observed a decrease in *Kidins220* levels in retinal and ON tissues compared to control littermates.

Ventriculomegaly, or hydrocephalus, characterized by an imbalance in CSF circulation, is a notable feature of *Kidins220*-deficient mice [19]. In humans, hydrocephalus is commonly associated with increased intracranial pressure due to excess of CSF, which elevates pressure in the arachnoid space surrounding the ON [44]. This pressure elevation can lead to papilledema, as observed in humans [45]. In the human ON, the lamina cribrosa (LC) region plays a crucial role in managing the transition between intraocular and intracranial pressure, due

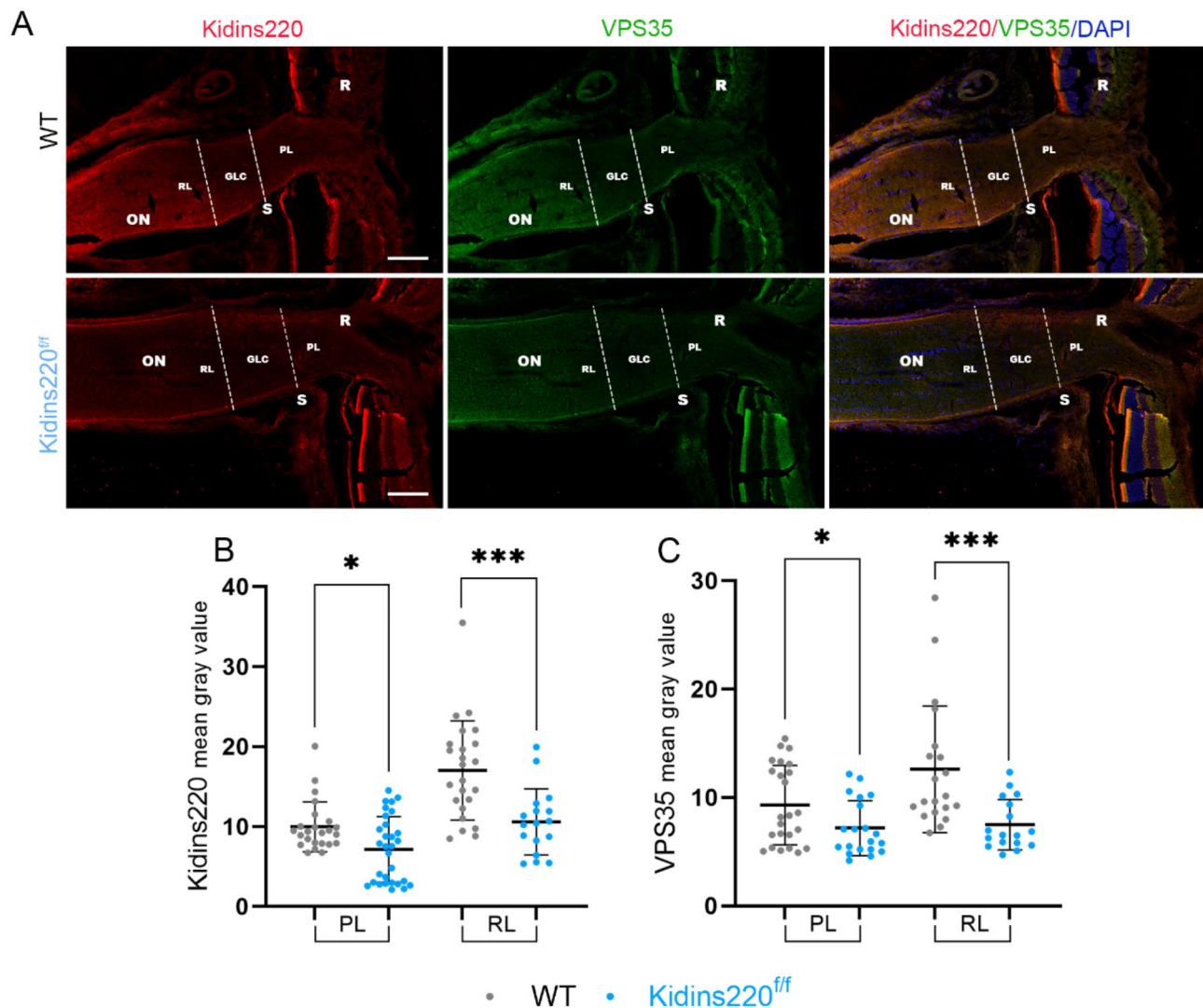


**Fig. 9** Kidins220 deficiency is accompanied by VPS35 deficits in the optic nerve. **(A)** Representative fluorescence microscopy images of Kidins220 (red) and VPS35 (green) immunolabelling in the optic nerve of WT and in *Kidins220<sup>ff</sup>* mice. Nuclei are labelled with DAPI (blue). **(B, C)** Quantitative analysis of the mean gray fluorescence value of Kidins220+ **(B)** and VPS35+ **(C)** immunostaining in WT and *Kidins220<sup>ff</sup>* mice. Data are mean  $\pm$  s.e.m.; each data point denotes an individual measure of the mean gray value of Kidins220+ and VPS35+ immunostaining in retinal sections of WT and *Kidins220<sup>ff</sup>* animals and were analyzed via Mann-Whitney U-test. \* $p < 0.05$ , \*\*\* $p < 0.001$ . Abbreviations: Retina (R), Sclera (S), Optic Nerve (ON), Prelaminar (PL), Glial Lamina Cribrosa (GLC), Retrolaminar (RL). Scale bar 100  $\mu$ m

to its biomechanical properties, allowing it to adapt to small pressure changes and prevent alterations in the axons of RGCs passing through it [46]. However, sustained increases in intracranial pressure can disrupt translaminar pressure in the LC region of the ON, causing it to bulge towards the eyeball and resulting in papilledema [47, 48]. Additionally, this elevated intracranial pressure compresses RGC axons and blood vessels passing through the LC, causing stasis in axoplasmic flow and fluid efflux from the vessels [47, 49]. In contrast, papilledema was not observed in our examination of 3-month-old *Kidins220<sup>ff</sup>* deficient mice using fundus examination or OCT studies. This discrepancy could be due to the potential development of papilledema at an older age

in our animal model or anatomical differences between the human and mouse ON. Unlike humans, mice lack a connective tissue in the LC, that is instead composed of astrocytes. This structural variation may confer different biomechanical properties [50], making the mouse GLC more elastic and less prone to anterior protrusion, thus avoiding visible manifestations of papilledema. Consistent with the lack of papilledema in our hydrocephalus mice, an *E2f5<sup>-/-</sup>* hydrocephalus mouse model, where elimination of *E2f5* gene leads to excessive CSF production, also does not present this condition [51]. In addition, the more flexible properties of mice astrocytic GLC could result in reduced mechanical damage to axons and vessels passing through this region of the ON, thereby

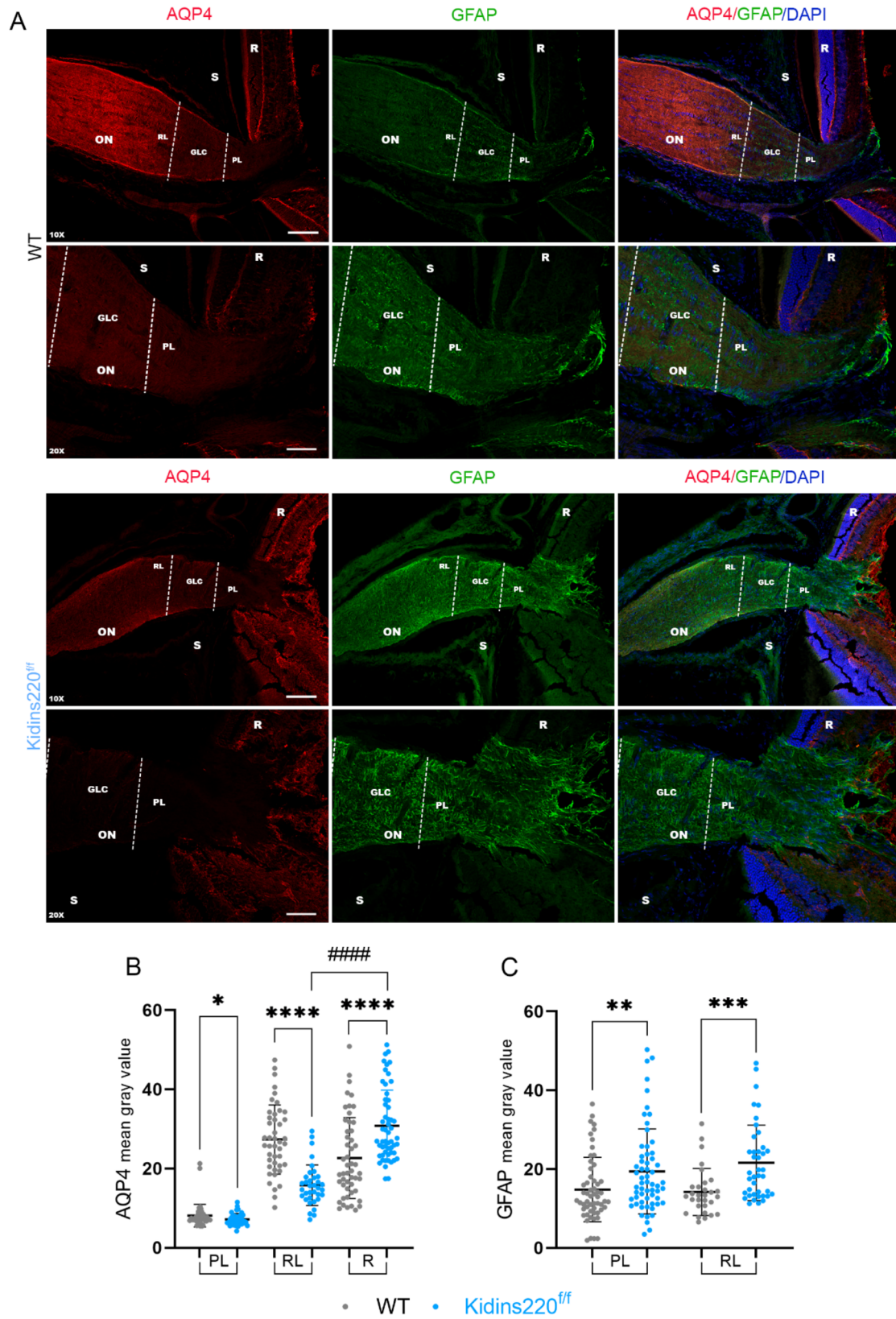


**Fig. 10** (See legend on next page.)

(See figure on previous page.)

**Fig. 10** The optic nerve of *Kidins220*-deficient mice exhibits increased GFAP expression with decreased AQP4 content. **(A)** Representative fluorescence microscopy images of AQP4 (red) and GFAP (green) immunostaining in the optic nerve of WT and *Kidins220*<sup>ff</sup> animals. Nuclei are labelled with DAPI (blue). **(B, C)**. Quantitative analysis of the mean gray fluorescence value of AQP4+ **(B)** and GFAP+ **(C)** immunostaining in WT and *Kidins220*<sup>ff</sup> mice. Data are mean ± s.e.m.; each data point denotes an individual measure of the mean gray value of AQP4+ and GFAP+ immunostaining in retinal sections of WT and *Kidins220*<sup>ff</sup> animals and were analyzed via Mann-Whitney U-test, \**p* < 0.05, \*\**p* < 0.01, \*\*\**p* < 0.001, \*\*\*\**p* < 0.0001; or Wilcoxon W-test, #####*p* < 0.0001. Abbreviations: Retina (R), Sclera (S), Optic Nerve (ON), Prelaminar (PL), Glial Lamina Cribrosa (GLC), Retrolaminar (RL). Upper panels: Scale bar 100 μm (10X); Lower panels: Scale bar 50 μm (20X)

reducing tissue edema. This increased flexibility may be associated with decreased RGC mortality, consistent with our observations. In our analysis, we did not detect significant differences in the number of Brn3a + RGCs or in the expression of the apoptosis marker cleaved caspase-3 in *Kidins220*<sup>ff</sup> mice compared to WT mice. These results align with findings in *E2f5*<sup>-/-</sup> hydrocephalus mice, where no changes were recorded in the thickness of the RGC layer or the NFL [51].

Increased intracranial pressure in the LC may result in an imbalance in translaminal pressure, potentially affecting the retinal fluid elimination system through the ocular glymphatic system. In the eye, the glymphatic system initiates with the aqueous humor which reaches the retina via the vitreous humor and mixes with the retinal interstitial fluid. Excess fluid is then transported by the axons of RGCs through the LC barrier, accumulating in perivenous spaces supported by AQP4 channels. From there, the fluid is directed towards the dural and cervical lymphatic vessels [52, 53]. This process is partially driven by the intraocular-intracranial pressure difference. If this mechanism malfunctions, fluid may accumulate in the retina. However, in *Kidins220*<sup>ff</sup> mice, no evidence of fluid accumulation in the retina is observed. OCT examination reveals no retinal thickening, whether analyzing total retinal or NFL thickness. These findings are consistent with observations in the *E2f5*<sup>-/-</sup> hydrocephalus mouse model, where histological analyses of various retinal layers, including the ONL, INL, RGC layer, and NFL, showed no significant changes [51]. Therefore, in hydrocephalus mice, fluid accumulation in the retina might be cleared through alternative pathways.

In contrast to the reduction in AQP4 levels in astrocytes and ependymocytes lining the brain lateral ventricles we have previously observed in *Kidins220*<sup>ff</sup> mice [19], the retina of these animals presents increased AQP4 levels, mainly in Müller glia. Müller cells play a crucial role in regulating water balance in the retina by removing water excess towards the vessels and vitreous humor [32, 34, 54, 55]. An increase in AQP4 in the retina of *Kidins220*<sup>ff</sup> mice could contribute to eliminating excess retinal fluid through Müller glia, thereby preventing its accumulation.

Differing markedly to the retina, AQP4 levels decrease in the ON of *Kidins220*<sup>ff</sup> animals. Astrocytes composing the ON GLC lack AQP4 [27], as we have also observed in this report. This condition may be necessary to limit

fluid transfer between the perivascular space and the ON in this area, where maintaining a pressure difference is essential. Furthermore, the absence of AQP4 in these GLC astrocytes could guide axonal fluid transport by restricting water movement through alternative routes within the astrocytes [53]. Overall, our data suggest a conserved pathway regulating AQP4 through *Kidins220* and the retromer in ependymocytes, and astrocytes from the brain and the ON, but different in the retina.

While retinal thickness and vascularity remain unchanged, *Kidins220*-deficient retinas show increased GFAP expression in astrocytes, increased vimentin expression in astrocytes and Müller glia, and an increase in the number and phagocytic activity of microglia. However, *Kidins220* deficiency is not associated with loss of RGCs or decreases in their survival, a phenomenon that might be anticipated given the role of *Kidins220* in promoting neuronal survival pathways [17]. It is possible that the changes undergone by astrocytes and Müller cells and microglia triggered in response to hydrocephalus damage aim to maintain retinal homeostasis by upregulating AQP4 in Müller glia and astrocytes facilitating fluid elimination towards vessels and vitreous humor [56], thereby preventing retinal edema formation. In addition, mechanical stress due to intracranial pressure could cause adjustments in astrocytes in the GLC through integrin-like mechanosensors [47]. As astrocytes form networks connected by gap junctions, they could transmit these alterations to retinal astrocytes [57]. The modifications of microglial cells in the retinas of *Kidins220*<sup>ff</sup> mice could be triggered by astrocyte changes. After damage, astrocytes generate cytokines and chemokines such as CCL2, CXCL1, CXCL10, GM-CSF, and IL-6, and molecules such as the C3 complement factor, which induce alterations in microglial cells [58]. In addition, the heightened phagocytic activity of microglia could suggest a need to clear accumulated debris in the retina. Future investigations in *Kidins220*<sup>ff</sup> animals will elucidate whether this phenomenon could be attributed to a potential malfunction of their glymphatic system of waste clearance.

In *Kidins220*<sup>ff</sup> hydrocephalus mice, the deficiency of *Kidins220* results in negative regulation of the SNX27-retromer, leading to lysosomal degradation of AQP4 [19]. This decrease in VPS35, the key component of the SNX27-retromer complex, and in AQP4, as previously observed in brain astrocytes and in ependymal cells of

Kidins220-deficient mice [19], is also evident in their ON. Given the retina is an extension of the brain, a similar regulatory mechanism was anticipated in retinal tissue. However, while our examination of the retina of *Kidins220<sup>ff</sup>* animals revealed reduced levels of Kidins220 and lower expression of VPS35, we surprisingly observed an increase in AQP4 expression. In the retina, Kidins220 exhibits widespread labeling across various retinal layers, with a notable presence in the GCL. This pattern aligns with previous findings in *Xenopus laevis*, where Kidins220 was primarily expressed in RGCs, as well as in other retinal regions such as the photoreceptor layer and the ON [59]. Similarly, VPS35 shows diffuse staining throughout the retina, with increased intensity in the GCL, consistent with previous studies identifying VPS35 predominantly in RGCs, amacrine cells, and astrocytes in the mouse retina [60]. Interestingly, the pronounced downregulation of Kidins220 and VPS35 in the retina of Kidins220-deficient mice is more evident in RGCs compared to other retinal cells, particularly in Müller glia where AQP4 upregulation is more prominent. One plausible explanation for these findings is that the levels and function of the retromer are tightly controlled in Müller cells to ensure their crucial role in maintaining water homeostasis, thereby preserving the viability of RGCs and overall visual health.

In humans, *KIDINS220* gene pathogenic variants are associated with SINO syndrome, hydrocephalus and ventriculomegaly [23–25]. In addition to nystagmus, less frequent ocular manifestations, such as strabismus/esotropia, have been reported in recently identified SINO syndrome cases [25]. Future studies utilizing OCT and OCTA in individuals with SINO syndrome and ventriculomegaly will be essential in determining whether different pathogenic variants correlate with retinal alterations and papilledema. Additionally, these investigations will provide insights into the potential impact of these changes on visual performance, thereby enhancing our understanding of the ocular manifestations of SINO syndrome and guiding future treatment approaches aimed at enhancing the quality of life of those affected.

#### Abbreviations

ARMS	Ankyrin-Repeat Rich Membrane Spanning
AQP4	Aquaporin-4
AQPs	Aquaporins
CSF	Cerebrospinal Fluid
FV	Fourth Ventricle
GCL	Ganglion Cell Layer
GFAP	Glial Fibrillary Acidic Protein
GCL	Glial Lamina Cribrosa
iNPH	Idiopathic Normal Pressure Hydrocephalus
ICL	Inner Complex Layer
IPL	Inner Plexiform Layer
Kidins220	Kinase D Interacting Substrate of 220 kDa
LC	Lamina Cribrosa
LV	Lateral Ventricle
NFL	Nerve Fiber Layer

ON	Optic Nerve
ONH	Optic Nerve Head
OCT	Optical Coherence Tomography
OCTA	Optical Coherence Tomography Angiography
OPL	Outer Plexiform Layer
OS	Outer Segment Layers
PL	Prelaminar
RGC	Retinal Ganglion Cells
RNFL	Retinal Nerve Fiber Layer
RL	Retrolaminar
SNX27	Sorting Nexin 27
SINO	Spastic Paraplegia, Intellectual Disability, Nystagmus, And Obesity Syndrome
SD-OCT	Spectral-Domain Optical Coherence Tomography
SA	Sylvius Aqueduct
TV	Third Ventricle
VPS35	Vacuolar Protein Sorting 35

#### Supplementary Information

The online version contains supplementary material available at <https://doi.org/10.1186/s12987-025-00626-z>.

Supplementary Material 1  
 Supplementary Material 2  
 Supplementary Material 3  
 Supplementary Material 4  
 Supplementary Material 5  
 Supplementary Material 6  
 Supplementary Material 7

#### Acknowledgements

Authors would like to thank Desiree Contreras and Madalin Georgian Olaeru for their valuable technical assistance. Our special thanks to the excellent technical support of the Biomedical MRI Sebastián Cerdán Service and the Animal care and Confocal Microscopy facilities at the IBM (CSIC-UAM). We also acknowledge the CSIC network of Rare Diseases (RER-CSIC).

#### Author contributions

TI, AIR, JJS, RdH and JMR conceived and designed the experiments, interpreted the data and wrote the paper with input from all authors. JAF-A, AS-G, ES-G, CL-M, LSMP, JAM, ILC, LEH, LSP, MPS-C and M.S. performed experiments, analyzed, interpreted and discussed results. All authors approved submission of this work.

#### Funding

LS-P is currently supported by a Predoctoral Fellowship (CT82/20-CT83/20) from the Complutense University of Madrid. JAM is currently supported by a Predoctoral Fellowship (CT58/21-CT59/21) from the Complutense University of Madrid. TI was supported by grants PID2020-115218RB-I00, funded by MCIN/AEI/10.13039/501100011000, and PID2023-153284OB-I00, funded by MCIU/AEI/10.13039/501100011000 and by ERDF/EU, and CB06/05/1122 Centro de Investigación Biomédica en Red de Enfermedades Neurodegenerativas (CIBERNED), Instituto de Salud Carlos III (ISCIII), Spain, funded by MCIU and supported in part by "ERDF A way of making Europe" funds. AS-G and MPS-C were supported by contracts associated to PID2020-115218RB-I00 and PID2023-153284OB-100 grants. LSMP was supported by a PhD training contract (PRE2018-086989) associated to grant SAF2017-88885-R, and by PID2020-115218RB-I00 and PID2023-153284OB-100 grants. MS was contracted by CIBERNED (ISCIII).

#### Data availability

The datasets generated and/or analyzed during the current study are available from the corresponding authors on reasonable request.

## Declarations

### Ethics approval and consent to participate

Not applicable.

### Consent for publication

Not applicable.

### Competing interests

The authors declare no competing interests.

### Author details

<sup>1</sup>Ramon Castroviejo Institute for Ophthalmic Research, Complutense University of Madrid, Madrid 28040, Spain

<sup>2</sup>Health Research Institute of the Hospital Clínico San Carlos (IdISSC), Madrid, Spain

<sup>3</sup>Department of Immunology, Ophthalmology and ENT, School of Medicine, Complutense University of Madrid, Madrid 28040, Spain

<sup>4</sup>Department of Immunology, Ophthalmology and ENT, Faculty of Optics and Optometry, Complutense University of Madrid, Madrid 28040, Spain

<sup>5</sup>Instituto de Investigaciones Biomédicas Sols-Morreale (IIBM), Consejo Superior de Investigaciones Científicas-Universidad Autónoma de Madrid (CSIC-UAM), Madrid 28029, Spain

<sup>6</sup>Centro de Investigación Biomédica en Red de Enfermedades Neurodegenerativas (CIBERNED), Instituto de Salud Carlos III (ISCIII), Madrid 28029, Spain

Received: 11 September 2024 / Accepted: 23 January 2025

Published online: 12 February 2025

## References

- Mak E, Su L, Williams GB, Firbank MJ, Lawson RA, Yarnall AJ et al. Longitudinal whole-brain atrophy and ventricular enlargement in nondemented Parkinson's disease. *Neurobiol Aging* [Internet]. 2017;55:78–90. Available from: <https://www.sciencedirect.com/science/article/pii/S0197458017300830>
- Nestor SM, Rupsingh R, Borrie M, Smith M, Accomazzi V, Wells JL et al. Ventricular enlargement as a possible measure of Alzheimer's disease progression validated using the Alzheimer's disease neuroimaging initiative database. *Brain* [Internet]. 2008 Sep [cited 2024 Feb 1];131(Pt 9):2443–54. Available from: <https://pubmed.ncbi.nlm.nih.gov/18669512/>
- Kempton MJ, Stahl D, Williams SCR, DeLisi LE. Progressive lateral ventricular enlargement in schizophrenia: a meta-analysis of longitudinal MRI studies. *Schizophr Res*. 2010;120(1–3):54–62.
- Feng X, Papadopoulos MC, Liu J, Li L, Zhang D, Zhang H et al. Sporadic obstructive hydrocephalus in Aqp4 null mice. *J Neurosci Res* [Internet]. 2009 Apr 1 [cited 2024 Apr 24];87(5):1150–5. Available from: <https://onlinelibrary.wiley.com/doi/full/https://doi.org/10.1002/jnr.21927>
- Bloch O, Auguste KJ, Manley GT, Verkman AS. Accelerated progression of kaolin-induced hydrocephalus in aquaporin-4-deficient mice. *Journal of Cerebral Blood Flow and Metabolism* [Internet]. 2006 Dec 8 [cited 2024 Apr 24];26(12):1527–37. Available from: <https://journals.sagepub.com/doi/full/https://doi.org/10.1038/sj.jcbfm.9600306>
- Iliff JJ, Wang M, Liao Y, Plogg BA, Peng W, Gundersen GA et al. A paravascular pathway facilitates CSF flow through the brain parenchyma and the clearance of interstitial solutes, including amyloid  $\beta$ . *Sci Transl Med* [Internet]. 2012 Aug 15 [cited 2024 Apr 24];4(147). Available from: <https://www.science.org/doi/https://doi.org/10.1126/scitranslmed.3003748>
- Haj-Yasein NN, Vindedal GF, Eilert-Olsen M, Gundersen GA, Skare Ø, Laake P et al. Glial-conditional deletion of aquaporin-4 (Aqp4) reduces blood–brain water uptake and confers barrier function on perivascular astrocyte endfeet. *Proceedings of the National Academy of Sciences* [Internet]. 2011 Oct 25 [cited 2024 Apr 24];108(43):17815–20. Available from: <https://www.pnas.org/doi/abs/https://doi.org/10.1073/pnas.1110655108>
- Iglesias T, Cabrera-Poch N, Mitchell MP, Naven TJP, Rozengurt E, Schiavo G. Identification and cloning of Kidins220, a novel neuronal substrate of protein kinase D. *Journal of Biological Chemistry* [Internet]. 2000 Dec 22 [cited 2024 Apr 24];275(51):40048–56. Available from: <http://www.jbc.org/article/S0021925819557349/fulltext>
- Kong H, Boulter J, Weber JL, Lai G, Chao MV. An evolutionarily conserved transmembrane protein that is a novel downstream target of neurotrophin and ephrin receptors. *J Neurosci* [Internet]. 2001 Jan 1 [cited 2024 Apr 24];21(1):176–85. Available from: <https://pubmed.ncbi.nlm.nih.gov/11150334/>
- Scholz-Starke J, Cesca F. Stepping Out of the Shade: Control of Neuronal Activity by the Scaffold Protein Kidins220/ARMS. *Front Cell Neurosci* [Internet]. 2016 Mar 14 [cited 2024 Apr 24];10(MAR2016). Available from: <https://pubmed.ncbi.nlm.nih.gov/27013979/>
- Neubrand VE, Cesca F, Benfenati F, Schiavo G. Kidins220/ARMS as a functional mediator of multiple receptor signalling pathways. *J Cell Sci* [Internet]. 2012 [cited 2024 Apr 24];125(Pt 8):1845–54. Available from: <https://pubmed.ncbi.nlm.nih.gov/22562556/>
- del Puerto A, Lopez-Fonseca C, Simón-García A, Martí-Prado B, Barrios-Muñoz AL, Pose-Utrilla J et al. Kidins220 sets the threshold for survival of neural stem cells and progenitors to sustain adult neurogenesis. *Cell Death Dis* [Internet]. 2023 Aug 1 [cited 2024 Apr 24];14(8). Available from: <https://pubmed.ncbi.nlm.nih.gov/37542079/>
- Gamir-Morralla A, López-Menéndez C, Ayuso-Dolado S, Tejada GS, Montaner J, Rosell A et al. Development of a neuroprotective peptide that preserves survival pathways by preventing Kidins220/ARMS calpain processing induced by excitotoxicity. *Cell Death Dis* [Internet]. 2015 [cited 2024 Apr 24];6(10). Available from: <https://pubmed.ncbi.nlm.nih.gov/26492372/>
- Sebastián-Serrano Á, Simón-García A, Belmonte-Alfaro A, Pose-Utrilla J, Santos-Galindo M, del Puerto A et al. Differential regulation of Kidins220 isoforms in Huntington's disease. *Brain Pathol* [Internet]. 2020 Jan 1 [cited 2024 Apr 24];30(1):120–36. Available from: <https://pubmed.ncbi.nlm.nih.gov/31264746/>
- Gamir-Morralla A, Belbin O, Fortea J, Alcolea D, Ferrer I, Lleó A et al. Kidins220 Correlates with Tau in Alzheimer's Disease Brain and Cerebrospinal Fluid. *J Alzheimers Dis* [Internet]. 2017 [cited 2024 Apr 24];55(4):1327–33. Available from: <https://pubmed.ncbi.nlm.nih.gov/27858709/>
- López-menéndez C, Gamir-morralla A, Jurado-arjona J, Higuero AM, Campanero MR, Ferrer I et al. Kidins220 accumulates with tau in human Alzheimer's disease and related models: modulation of its calpain-processing by GSK3 $\beta$ /PP1 imbalance. *Hum Mol Genet* [Internet]. 2013 Feb [cited 2024 Apr 24];22(3):466–82. Available from: <https://pubmed.ncbi.nlm.nih.gov/23118350/>
- López-Menéndez C, Gascón S, Sobrado M, Vidaurre OG, Higuero AM, Rodríguez-Peña Á et al. Kidins220/ARMS downregulation by excitotoxic activation of NMDARs reveals its involvement in neuronal survival and death pathways. *J Cell Sci* [Internet]. 2009 Oct 1 [cited 2024 Apr 24];122(Pt 19):3554–65. Available from: <https://pubmed.ncbi.nlm.nih.gov/19759287/>
- López-Benito S, Sánchez-Sánchez J, Brito V, Calvo L, Lisa S, Torres-Valle M et al. Regulation of BDNF Release by ARMS/Kidins220 through Modulation of Synaptotagmin-IV Levels. *Journal of Neuroscience* [Internet]. 2018 Jun 6 [cited 2024 May 27];38(23):5415–28. Available from: <https://www.jneurosci.org/content/38/23/5415>
- del Puerto A, Pose-Utrilla J, Simón-García A, López-Menéndez C, Jiménez AJ, Porlan E et al. Kidins220 deficiency causes ventriculomegaly via SNX27-retromer-dependent AQP4 degradation. *Mol Psychiatry* [Internet]. 2021 Nov 1 [cited 2024 Jan 30];26(11):6411–26. Available from: <https://pubmed.ncbi.nlm.nih.gov/34002021/>
- Steinberg F, Gallon M, Winfield M, Thomas EC, Bell AJ, Heesom KJ et al. A global analysis of SNX27-retromer assembly and cargo specificity reveals a function in glucose and metal ion transport. *Nat Cell Biol* [Internet]. 2013;15(5):461–71. Available from: <https://doi.org/10.1038/ncb2721>
- Kranz TM, Goetz RR, Walsh-Messinger J, Goetz D, Antonius D, Dolgalev I et al. Rare variants in the neurotrophin signaling pathway implicated in schizophrenia risk. *Schizophr Res* [Internet]. 2015 Oct 1 [cited 2024 Feb 1];168(1–2):421–8. Available from: <https://pubmed.ncbi.nlm.nih.gov/26215504/>
- Malaspina D, Kranz TM, Heguy A, Harroch S, Mazgaj R, Rothman K et al. Frontal neuronal integrity predicts symptoms and cognition in schizophrenia and is sensitive to genetic heterogeneity. *Schizophr Res* [Internet]. 2016 Apr 1 [cited 2024 Feb 1];172(1–3):94–100. Available from: <https://pubmed.ncbi.nlm.nih.gov/26925801/>
- Mero IL, Mørk HH, Sheng Y, Blomhoff A, Opheim GL, Erichsen A et al. Homozygous KIDINS220 loss-of-function variants in fetuses with cerebral ventriculomegaly and limb contractures. *Hum Mol Genet* [Internet]. 2017;26(19):3792–6. Available from: <https://doi.org/10.1093/hmg/ddx263>
- Josifova DJ, Monroe GR, Tessoro F, de Graaff E, van der Zwaag B, Mehta SG et al. Heterozygous KIDINS220/ARMS nonsense variants cause spastic paraplegia, intellectual disability, nystagmus, and obesity. *Hum Mol Genet*

- [Internet]. 2016 Jun 1 [cited 2024 Feb 1];25(11):2158–67. Available from: <https://pubmed.ncbi.nlm.nih.gov/27005418/>
25. Alstrup M, Cesca F, Krawczun-Rygmaczewska A, López-Menéndez C, Pose-Utrilla J, Castberg FC et al. Refining the phenotype of SINO syndrome: A comprehensive cohort report of 14 novel cases. *Genet Med* [Internet]. 2024 Jul [cited 2024 Sep 11];101219. Available from: <https://pubmed.ncbi.nlm.nih.gov/39033379/>
  26. Rathnasamy G, Foulds WS, Ling EA, Kaur C. Retinal microglia—A key player in healthy and diseased retina. *Progress in Neurobiology*. Volume 173. Elsevier Ltd; 2019. pp. 18–40.
  27. Nagelhus EA, Veruki ML, Torp R, Haug FM, Laake JH, Nielsen S et al. Aquaporin-4 water channel protein in the rat retina and optic nerve: polarized expression in Müller cells and fibrous astrocytes. *J Neurosci* [Internet]. 1998 Apr 1 [cited 2024 Feb 1];18(7):2506–19. Available from: <https://pubmed.ncbi.nlm.nih.gov/9502811/>
  28. Iandiev I, Pannicke T, Biedermann B, Wiedemann P, Reichenbach A, Bringmann A. Ischemia-reperfusion alters the immunolocalization of glial aquaporins in rat retina. *Neurosci Lett*. 2006;408(2):108–12.
  29. Iandiev I, Pannicke T, Reichel MB, Wiedemann P, Reichenbach A, Bringmann A. Expression of aquaporin-1 immunoreactivity by photoreceptor cells in the mouse retina. *Neurosci Lett*. 2005;388(2):96–9.
  30. Tenckhoff S, Hollborn M, Kohen L, Wolf S, Wiedemann P, Bringmann A. Diversity of aquaporin mRNA expressed by rat and human retinas. *Neuroreport* [Internet]. 2005;16(1). Available from: [https://journals.lww.com/neuroreport/fulltext/2005/01190/diversity\\_of\\_aquaporin\\_mrna\\_expressed\\_by\\_rat\\_and\\_hu.13.aspx](https://journals.lww.com/neuroreport/fulltext/2005/01190/diversity_of_aquaporin_mrna_expressed_by_rat_and_hu.13.aspx)
  31. Nagelhus EA, Horio Y, Inanobe A, Fujita A, Haug FM, Nielsen S et al. Immunogold Evidence Suggests That Coupling of K Siphoning and Water Transport in Rat Retinal Müller Cells Is Mediated by a Coenrichment of Kir4.1 and AQP4 in Specific Membrane Domains. *Glia* [Internet]. 1999 [cited 2024 Feb 2];26:47–54. Available from: <https://onlinelibrary.wiley.com/doi/10.1002/glia.20661>
  32. Schey KL, Wang Z, Wenke L, Qi J. Aquaporins in the eye: expression, function, and roles in ocular disease. *Biochimica et Biophysica Acta (BBA) - Gen Subj*. 2014;1840(5):1513–23.
  33. Tong XJ, Akdemir G, Wadhwa M, Verkman AS, Smith AJ. Large molecules from the cerebrospinal fluid enter the optic nerve but not the retina of mice. *Fluids Barriers CNS* [Internet]. 2024 Dec 1 [cited 2024 May 27];21(1):1–12. Available from: <https://link.springer.com/articles/https://doi.org/10.1186/s12987-023-00506-4>
  34. Bringmann A, Pannicke T, Grosche J, Francke M, Wiedemann P, Skatchkov SN, et al. Müller cells in the healthy and diseased retina. *Prog Retin Eye Res*. 2006;25(4):397–424.
  35. Li J, Patil RV, Verkman AS. Mildly abnormal retinal function in transgenic mice without Müller cell Aquaporin-4 Water channels. *Invest Ophthalmol Vis Sci*. 2002;43(2):573–9.
  36. Cesca F, Yabe A, Spencer-Dene B, Scholz-Starke J, Medrihan L, Maden CH et al. Kidins220/ARMS mediates the integration of the neurotrophin and VEGF pathways in the vascular and nervous systems. *Cell Death & Differentiation* 2012 19:2 [Internet]. 2011 Nov 3 [cited 2024 Apr 24];19(2):194–208. Available from: <https://www.nature.com/articles/cdd2011141>
  37. Salobar-García E, López-Cuenca I, Sánchez-Puebla L, de Hoz R, Fernández-Albarral JA, Ramírez AI, et al. Retinal thickness changes over time in a murine AD Model APPNL-F/NL-F. *Front Aging Neurosci*. 2021;12:625642.
  38. Zudaire E, Gambardella L, Kurcz C, Vermeren S. A computational tool for quantitative analysis of vascular networks. *PLoS ONE*. 2011;6(11).
  39. López-Cuenca I, Salobar-García E, Sánchez-Puebla L, Espejel E, Del Arco LG, Rojas P, et al. Retinal vascular study using OCTA in subjects at high genetic risk of developing Alzheimer's Disease and Cardiovascular Risk factors. *J Clin Med*. 2022;11(11):1–18.
  40. de Gracia P, Gallego BI, Rojas B, Ramírez AI, de Hoz R, Salazar JJ, et al. Automatic counting of microglial cells in healthy and glaucomatous mouse retinas. *PLoS ONE*. 2015;10(11):e0143278.
  41. De Bellis M, Pisani F, Mola MG, Rosito S, Simone L, Buccoliero C et al. Translational readthrough generates new astrocyte AQP4 isoforms that modulate supramolecular clustering, glial endfeet localization, and water transport. *Glia* [Internet]. 2017 May 1 [cited 2024 Dec 18];65(5):790–803. Available from: <https://onlinelibrary.wiley.com/doi/full/https://doi.org/10.1002/glia.23126>
  42. López-Menéndez C, Simón-García A, Gamir-Morralla A, Pose-Utrilla J, Luján R, Mochizuki N et al. Excitotoxic targeting of Kidins220 to the Golgi apparatus precedes calpain cleavage of Rap1-activation complexes. *Cell Death Dis* [Internet]. 2019 Jul 1 [cited 2024 Apr 24];10(7). Available from: <https://pubmed.ncbi.nlm.nih.gov/31296845/>
  43. Nicchia GP, Rossi A, Nudel U, Svelto M, Frigeri A. Dystrophin-dependent and -independent AQP4 pools are expressed in the mouse brain. *Glia* [Internet]. 2008 Jun 1 [cited 2024 Dec 18];56(8):869–76. Available from: <https://onlinelibrary.wiley.com/doi/full/https://doi.org/10.1002/glia.20661>
  44. Rigi M, Almarzouqi SJ, Morgan ML, Lee AG. Papilledema: epidemiology, etiology, and clinical management. *Eye Brain* [Internet]. 2015 Aug 17 [cited 2024 Jan 30];7:47–57. Available from: <https://pubmed.ncbi.nlm.nih.gov/28539794/>
  45. Lee HJ, Phi JH, Kim SK, Wang KC, Kim SJ. Papilledema in children with hydrocephalus: incidence and associated factors. *J Neurosurg Pediatr* [Internet]. 2017 Jun 1 [cited 2024 Jan 30];19(6):627–31. Available from: <https://pubmed.ncbi.nlm.nih.gov/28387641/>
  46. Sigal IA, Ethier CR. Biomechanics of the optic nerve head. *Exp Eye Res*. 2009;88:799–807.
  47. Salazar JJ, Ramírez AI, De Hoz R, Salobar-García E, Rojas P, Fernández-Albarral JA, et al. Anatomy of the human optic nerve: structure and function. *Optic Nerve*. 2018;203:22–30.
  48. Sudhakar P, Commentary. Assessing the lamina cribrosa in idiopathic intracranial hypertension. *Indian J Ophthalmol* [Internet]. 2020 Jan 1 [cited 2024 Jan 30];68(1):168–9. Available from: <https://pubmed.ncbi.nlm.nih.gov/31856500/>
  49. Hayreh SS. Pathogenesis of optic disc edema in raised intracranial pressure. *Prog Retin Eye Res* [Internet]. 2016 Jan 1 [cited 2024 Jan 30];50:108–44. Available from: <https://pubmed.ncbi.nlm.nih.gov/26453995/>
  50. May CA, Lütjen-Drecoll E. Morphology of the Murine Optic nerve. *Invest Ophthalmol Vis Sci*. 2002;43(7):2206–12.
  51. Mccue RA. Effects of Hydrocephalus on Rodent Optic Nerve and Optic Disc. (Doctoral dissertation, Purdue University Graduate School). 2021.
  52. Mogensen FLH, Delle C, Nedergaard M. The Glymphatic System (En)during Inflammation. *International Journal of Molecular Sciences*. 2021, Vol 22, Page 7491 [Internet]. 2021 Jul 13 [cited 2024 Feb 1];22(14):7491. Available from: <https://www.mdpi.com/1422-0067/22/14/7491/html>
  53. Wang X, Lou N, Eberhardt A, Yang Y, Kusk P, Xu Q et al. An ocular glymphatic clearance system removes  $\beta$ -amyloid from the rodent eye. *Sci Transl Med* [Internet]. 2020 Mar 25 [cited 2024 Jan 31];12(536):3210. Available from: <https://www.science.org/doi/https://doi.org/10.1126/scitranslmed.aaw3210>
  54. Lai D, Wu Y, Shao C, Qiu Q. The Role of Müller Cells in Diabetic Macular Edema. *Invest Ophthalmol Vis Sci* [Internet]. 2023 Jul 3 [cited 2024 Feb 1];64(10):8–8. Available from: <https://doi.org/10.1167/iov.64.10.8>
  55. Verkman AS, Ruiz-Ederra J, Levin MH. Functions of aquaporins in the eye. *Prog Retin Eye Res*. 2008;27(4):420–33.
  56. de Hoz R, Rojas B, Ramírez AI, Salazar JJ, Gallego BI, Triviño A et al. Retinal Macroglial Responses in Health and Disease. *Biomed Res Int* [Internet]. 2016 May 18 [cited 2019 Jun 20];2016:2954721. Available from: <http://www.hindawi.com/journals/bmri/2016/2954721/>
  57. Ramírez JM, Triviño A, Ramírez AI, Salazar JJ, García-Sánchez J. Structural specializations of human retinal glial cells. *Vis Res*. 1996;36(14):2029–36.
  58. Ramírez AI, de Hoz R, Salobar-García E, Salazar JJ, Rojas B, Ajoy D, et al. The role of microglia in retinal neurodegeneration: Alzheimer's disease, Parkinson, and glaucoma. *Frontiers in Aging Neuroscience*. Volume 9. Frontiers; 2017. p. 214.
  59. Marracci S, Giannini M, Vitiello M, Andreazzoli M, Dente L. Kidins220/ARMS is dynamically expressed during *Xenopus laevis* development. *Int J Dev Biol* [Internet]. 2013 [cited 2024 Feb 1];57(9–10):787–92. Available from: <https://pubmed.ncbi.nlm.nih.gov/24307304/>
  60. Liu W, Tang FL, Erion J, Xiao H, Ye J, Xiong WC. Vps35 haploinsufficiency results in degenerative-like deficit in mouse retinal ganglion neurons and impairment of optic nerve injury-induced gliosis. *Mol Brain* [Internet]. 2014 Feb 11 [cited 2024 Feb 1];7(1). Available from: <https://pubmed.ncbi.nlm.nih.gov/24512632/>

## Publisher's note

Springer Nature remains neutral with regard to jurisdictional claims in published maps and institutional affiliations.